Available online at www.sciencedirect.com
ScienceDirect
Comput. Methods Appl. Mech. Engrg. 391 (2022) 114607
Computer methods in applied mechanics and engineering
www.elsevier.com/locate/cma

3D–0D closed-loop model for the simulation of cardiac biventricular electromechanics

Roberto Piersanti[a], Francesco Regazzoni[a,*], Matteo Salvador[a], Antonio F. Corno[b], Luca Dede'[a], Christian Vergara[c], Alfio Quarteroni[a,d]

[a] *MOX - Dipartimento di Matematica, Politecnico di Milano, P.zza Leonardo da Vinci 32, 20133 Milano, Italy*
[b] *Houston Children's Heart Institute, Hermann Children's Hospital University of Texas Health, McGovern Medical School, Houston, TX, USA*
[c] *LaBS, Dipartimento di Chimica, Materiali e Ingegneria Chimica "Giulio Natta", Politecnico di Milano, P.zza Leonardo da Vinci 32, 20133 Milano, Italy*
[d] *Mathematics Institute, École Polytechnique Fédérale de Lausanne, Av. Piccard, CH-1015, Lausanne, Switzerland (Professor Emeritus)*

Received 3 August 2021; received in revised form 24 November 2021; accepted 10 January 2022
Available online xxxx

Abstract

Two crucial factors for accurate numerical simulations of cardiac electromechanics, which are also essential to reproduce the synchronous activity of the heart, are: (i) accounting for the interaction between the heart and the circulatory system that determines pressures and volumes loads in the heart chambers; (ii) reconstructing the muscular fiber architecture that drives the electrophysiology signal and the myocardium contraction. In this work, we present a 3D biventricular electromechanical model coupled with a 0D closed-loop model of the whole cardiovascular system that addresses the two former crucial factors. With this aim, we introduce a boundary condition for the mechanical problem that accounts for the neglected part of the domain located on top of the biventricular basal plane and that is consistent with the principles of momentum and energy conservation. We also discuss in detail the coupling conditions behind the 3D and the 0D models. We perform electromechanical simulations in physiological conditions using the 3D–0D model and we show that our results match the experimental data of relevant mechanical biomarkers available in the literature. Furthermore, we investigate different arrangements in cross-fibers active contraction. We prove that an active tension along the sheet direction counteracts the myofiber contraction, while the one along the sheet-normal direction enhances the cardiac work. Finally, several myofiber architectures are analyzed. We show that a different fiber field in the septal area and in the transmural wall affects the pumping functionality of the left ventricle.

Keywords: Cardiac electromechanics; Cardiac fiber architecture; Multiphysics modeling; Finite Elements; 3D–0D coupling

1. Introduction

Over the years, computational models of cardiac electromechanics (EM) [1–7] have been developed with increasingly biophysical detail, by taking into account the interacting physical phenomena characteristic of the heart EM — electrophysiology, active contraction, mechanics [8–12]. However, most of the existing EM models refer to the left ventricle (LV) only [13–19] and neglect the important effects of the right ventricular deformation on

* Corresponding author.
E-mail address: francesco.regazzoni@polimi.it (F. Regazzoni).

https://doi.org/10.1016/j.cma.2022.114607

the heart pumping function [20]. Only recently, biventricular EM models [21–28] have been purposely developed. Two crucial factors for an accurate numerical simulation of the cardiac EM, which are also essential to reproduce the synchronous activity of the heart, are: (i) accounting for the interaction between the heart and the circulatory system and (ii) reconstructing the muscular fiber architecture.

The coupling between the circulatory system hemodynamics and the cardiac mechanics determines pressures and volumes in the heart chambers [14,28–32]. Typically, 3D EM models are coupled with Windkessel-type preload/afterload models for the circulatory system [33–38]. In these models, the different phases of the pressure–volume loop (PV-loop) are managed by solving different sets of differential equations, one for each phase [14, 39–41]. Still, more meaningful and physiologically sound interface conditions can be obtained by coupling the 3D EM model with a 0D closed-loop fluid dynamics model of the complete circulatory system for the whole cardiac cycle [15,42–45]. A further advantage of the latter approach is that closed-loop circulation models do not require to be adapted through the different phases of the cardiac cycle [5,28,30,46]. However, solving efficiently the coupling between the EM model and the closed-loop model for the whole cardiovascular system is a challenging task [28]. To the best of our knowledge, this coupled problem has been so far addressed only in a few works, namely [15,25,28,29].

The myocardial fibers play a key role in the electric signal propagation and in the myocardial contraction [47–51]. Due to the difficulty of reconstructing cardiac fibers from medical imaging, a widely used strategy for generating myofiber orientations in EM models relies on the so called Laplace–Dirichlet-Rule-Based-Methods (LDRBMs) [52–55], recently analyzed under a communal mathematical setting [47]. While it is well recognized that myofibers orientation is crucial for the construction of a realistic EM model, their architecture has been explored only in a few works and it is not fully understood [20,31,50,56,57]. Another crucial issue for the reconstruction of a suitable cardiac fiber architecture consists in considering the myofibers dispersion around a predominant direction [31,58–60]. Based on experimental measures [61], cross-fibers active tension has been introduced in [62–64] to model the contraction caused by dispersed myofibers. However, to the best of our knowledge, this aspect was addressed in EM models only in [17,65].

With the aim of facing the computational challenges formerly described, our contributions in this paper move along two strands: (i) on the one hand, we present a biophysically detailed 3D biventricular EM model coupled with a 0D closed-loop lumped parameters model for the hemodynamics of the whole circulatory system; (ii) on the other hand, we investigate the effect of different myofiber architectures, by considering three type of LDRBMs, on the biventricular EM. Specifically, we provide the mathematical formulation and the numerical framework of the coupled 3D–0D model carefully inspecting the coupling conditions of these heterogeneous models. We propose an effective boundary condition for the mechanical problem that accounts for the neglected part of the domain located above the biventricular basal plane and that fulfills the principles of momentum and energy conservation. We report the results of several electromechanical simulations in physiological conditions using the proposed 3D–0D model. Our results match the experimental data of relevant mechanical biomarkers available in the literature [66–72]. Furthermore, we study at which extent different configurations in cross-fibers active contraction, that surrogate the myofibers dispersion, affect the electromechanical simulations.

This paper is organized as follows. In Section 2 we briefly recall the fiber generation methods used to model the cardiac muscle fiber architecture in biventricular geometries. Moreover, we fully present the mathematical formulation for the closed-loop 3D–0D EM model. Then, in Section 3 we present the numerical approximation of the 3D–0D model along with the coupling strategy. In Section 4, we show the numerical results obtained with the proposed model. Finally, in Section 6 we draw our conclusions.

2. Mathematical models

In this section we provide a brief overview of the fiber generation methods used to reconstruct the cardiac muscle architecture in biventricular geometries (Section 2.1) and we fully present the 3D cardiac EM model for the human heart function together with a 0D model of the whole cardiovascular system (Section 2.2). Finally, we show the strategy to reconstruct the unloaded (i.e. stress-free) configuration (Section 2.3).

We denote by Ω_0 the computational domain in the reference configuration, see Fig. 1(a), representing the region occupied by the left and right ventricles, whose boundary $\partial\Omega_0$ is partitioned into the epicardium Γ_0^{epi}, the left $\Gamma_0^{\text{endo,LV}}$ and right $\Gamma_0^{\text{endo,RV}}$ endocardial surfaces and the biventricular base Γ_0^{base} (namely an artificial basal plane located well below the cardiac valves), so that we have $\partial\Omega_0 = \overline{\Gamma}_0^{\text{epi}} \cup \overline{\Gamma}_0^{\text{endo,lv}} \cup \overline{\Gamma}_0^{\text{endo,rv}} \cup \overline{\Gamma}_0^{\text{base}}$.

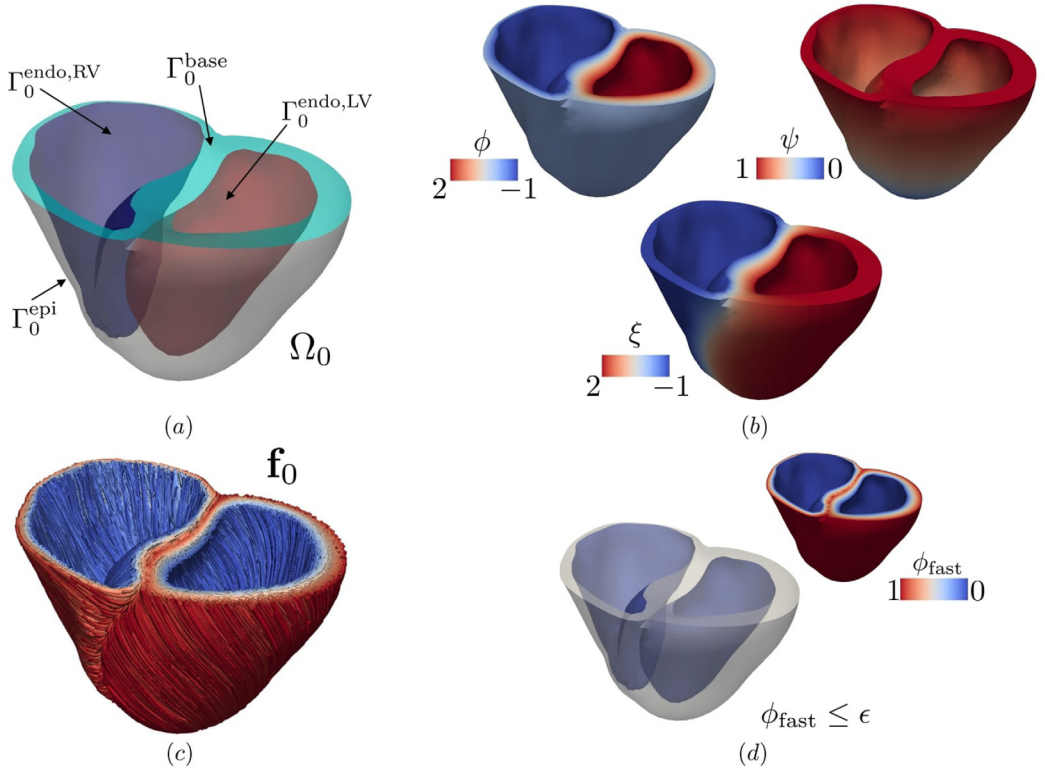

Fig. 1. Top left (a): representation of a realistic biventricular computational domain Ω_0 whose border is partitioned in Γ_0^{epi}, Γ_0^{base}, $\Gamma_0^{\text{endo,LV}}$ and $\Gamma_0^{\text{endo,RV}}$. Top Right (b): solutions of the Laplace problem (1) defining ϕ the transmural, ψ the apico-basal and ξ the inter-ventricular distances that are used to prescribe the myofiber orientations using LDRBM of type D-RBM. Bottom left (c): fiber field $\mathbf{f}_0$ obtained using D-RBM. Bottom right (d): ϕ_{fast} solution of the Laplace problem (1) used to build the fast endocardial layer $\phi_{\text{fast}} \leq \epsilon$ [73].

2.1. Fibers generation

To prescribe the cardiac muscle fiber architecture in the biventricular computational domain Ω_0, we use a particular class of Rule-Based-Methods (RBMs), known as Laplace–Dirichlet-Rule-Based-Methods (LDRBMs) [52,53,74]. Specifically, we consider three LDRBMs, respectively proposed by Rossi et al. (R-RBM) [19,55], Bayer et al. (B-RBM) [52] and Doste et al. (D-RBM) [54], that were recently reviewed in a communal mathematical description and extended to embed specific fiber directions for the right ventricle (RV) in [47].

LDRBMs define the transmural ϕ (from epicardium to endocardium), the apico-basal ψ (from apex to basal plane) and the inter-ventricular ξ (from the left to right endocardia) distances as the solutions of suitable Laplace boundary-value problems of the type

$$\begin{cases} -\Delta\chi = 0 & \text{in } \Omega_0, \\ \chi = \chi_{\text{a}} & \text{on } \Gamma_0^{\text{a}}, \\ \chi = \chi_{\text{b}} & \text{on } \Gamma_0^{\text{b}}, \\ \nabla\chi \cdot \mathbf{N} = 0 & \text{on } \Gamma_0^{\text{n}}, \end{cases} \tag{1}$$

where $\chi = \phi, \psi, \xi$ denotes a generic unknown, $\chi_{\text{a}}, \chi_{\text{b}} \in \mathbb{R}$ are suitable boundary data set on generic partitions of the boundary Γ_0^{a}, Γ_0^{b}, Γ_0^{n}, with $\overline{\Gamma}_0^{\text{a}} \cup \overline{\Gamma}_0^{\text{b}} \cup \overline{\Gamma}_0^{\text{n}} = \partial\Omega_0$ and $\mathbf{N}$ is defined as the outer normal vector, see Figs. 1(b). For each point of the biventricular domain, the transmural and apico-basal distances are used to build an orthonormal

local coordinate axial system $[\widehat{\boldsymbol{e}}_\ell, \widehat{\boldsymbol{e}}_\mathrm{n}, \widehat{\boldsymbol{e}}_\mathrm{t}]$ owing to $\widehat{\boldsymbol{e}}_\mathrm{t} = \frac{\nabla\phi}{\|\nabla\phi\|}$, $\widehat{\boldsymbol{e}}_\mathrm{n} = \frac{\nabla\psi - (\nabla\psi\cdot\widehat{\boldsymbol{e}}_\mathrm{t})\widehat{\boldsymbol{e}}_\mathrm{t}}{\|\nabla\psi - (\nabla\psi\cdot\widehat{\boldsymbol{e}}_\mathrm{t})\widehat{\boldsymbol{e}}_\mathrm{t}\|}$ and $\widehat{\boldsymbol{e}}_\ell = \widehat{\boldsymbol{e}}_\mathrm{n} \times \widehat{\boldsymbol{e}}_\mathrm{t}$, defined as the unit transmural, longitudinal and normal directions, respectively. Finally, the reference frame $[\widehat{\boldsymbol{e}}_\ell, \widehat{\boldsymbol{e}}_\mathrm{n}, \widehat{\boldsymbol{e}}_\mathrm{t}]$ is properly rotated with the purpose of defining the myofiber orientations:

$$[\widehat{\boldsymbol{e}}_\ell, \widehat{\boldsymbol{e}}_\mathrm{n}, \widehat{\boldsymbol{e}}_\mathrm{t}] \xrightarrow{\alpha_\mathrm{i}, \beta_\mathrm{i}} [\mathbf{f}_0, \mathbf{n}_0, \mathbf{s}_0], \quad \mathrm{i} = \mathrm{LV,RV},$$

where $\mathbf{f}_0$ is the fiber direction, $\mathbf{n}_0$ is the sheet-normal direction, $\mathbf{s}_0$ is the sheet direction, i = LV,RV refers to LV or RV, and α_i and β_i are suitable helical and sheetlet angles following linear relationships $\theta_\mathrm{i}(d_\mathrm{i}) = \theta_{\mathrm{epi,i}}(1-d_\mathrm{i}) + \theta_{\mathrm{endo,i}} d_\mathrm{i}$, (with $\theta = \alpha, \beta$ and i = LV,RV) in which $d_\mathrm{i} \in [0, 1]$ is the transmural normalized distance and $\theta_{\mathrm{endo,i}}$, $\theta_{\mathrm{epi,i}}$ are suitable prescribed rotation angles on the endocardium and epicardium, see Fig. 1(c). To prescribe different myofiber orientations for LV and RV, we employ the inter-ventricular distance ξ in which positive values of ξ identify the LV, whereas negative values refer to the RV [47]. Moreover, we define the normalized inter-ventricular distance $\hat{\xi} \in [0, 1]$ by rescaling ξ.

An example of LDRBM boundary-value solutions for the fiber generation procedure (of D-RBM type) is sketched in Fig. 1(b). For further details about LDRBMs we refer to [47].

2.2. 3D-0D closed-loop electromechanical model

We provide a detailed description of the multiphysics and multiscale 3D biventricular EM model coupled with a 0D closed-loop (lumped parameters) hemodynamic model of the whole cardiovascular system, including the heart blood flow. Our model features several extensions and novel additions with respect to the work [15,46], that is limited to the left ventricle. Our 3D–0D model is composed of four *core models* supplemented by a suitable coupling condition between the 3D and the 0D model. The core models are related to the different interplaying physical processes (at the molecular, cellular, tissue and organ levels) involved in the heart pumping function: cardiac electrophysiology ($\mathscr{E}$) [17,75–77], cardiomyocytes active contraction ($\mathscr{A}$) [19,78–82], tissue mechanics ($\mathscr{M}$) [83–86] and blood circulation ($\mathscr{C}$) [15,25,28,29,42,43,87]. The coupling condition is established by the volume conservation constraints ($\mathscr{V}$) [15].

The model unknowns are:

$$\begin{aligned} &u : \Omega_0 \times [0, T] \to \mathbb{R}, && \boldsymbol{w} : \Omega_0 \times [0, T] \to \mathbb{R}^{n_{\boldsymbol{w}}}, \\ &\mathbf{s} : \Omega_0 \times [0, T] \to \mathbb{R}^{n_{\mathbf{s}}}, && \mathbf{d} : \Omega_0 \times [0, T] \to \mathbb{R}^3, \qquad \boldsymbol{c} : [0, T] \to \mathbb{R}^{n_{\boldsymbol{c}}}, \\ &p_{\mathrm{LV}} : [0, T] \to \mathbb{R}, && p_{\mathrm{RV}} : [0, T] \to \mathbb{R}, \end{aligned}$$

where u is the transmembrane potential, $\boldsymbol{w}$ is the vector containing the ionic variables, which encodes the intracellular calcium concentration $w_{\mathrm{Ca}} = [\mathrm{Ca}^{2+}]_\mathrm{i}$. Moreover, $\mathbf{s}$ represents the vector of the state variables in the active force generation model, $\mathbf{d}$ is the mechanical displacement of the myocardium, $\boldsymbol{c}$ is the state vector of the circulation model (including pressures, volumes and fluxes of the different compartments composing the vascular network), p_{LV} and p_{RV} are the left and right ventricular pressures, respectively.

Given the computational domain Ω_0 and the time interval $t \in (0, T]$, our complete 3D–0D model reads:

$$(\mathscr{E}) \begin{cases} J\chi_\mathrm{m}\left[C_\mathrm{m}\dfrac{\partial u}{\partial t} + \mathcal{I}_{\mathrm{ion}}(u, \boldsymbol{w})\right] - \nabla\cdot(J\mathbf{F}^{-1}\boldsymbol{D}\,\mathbf{F}^{-T}\nabla u) = J\chi_\mathrm{m}\mathcal{I}_{\mathrm{app}}(t) & \text{in } \Omega_0 \times (0, T], \quad (2.1) \\ \dfrac{\partial \boldsymbol{w}}{\partial t} - \boldsymbol{H}(u, \boldsymbol{w}) = \mathbf{0} & \text{in } \Omega_0 \times (0, T], \quad (2.2) \\ \left(J\mathbf{F}^{-1}\boldsymbol{D}\,\mathbf{F}^{-T}\nabla u\right)\cdot\mathbf{N} = 0 & \text{on } \partial\Omega_0 \times (0, T], \quad (2.3) \end{cases}$$

$$(\mathscr{A}) \frac{\partial \mathbf{s}}{\partial t} = \boldsymbol{K}(\mathbf{s}, w_{\mathrm{Ca}}, SL) \qquad \text{in } \Omega_0 \times (0, T], \quad (2.4)$$

$$(\mathscr{M})\begin{cases}\rho_s \dfrac{\partial^2 \mathbf{d}}{\partial t^2} - \nabla \cdot \mathbf{P}(\mathbf{d}, T_a(\mathbf{s}, \boldsymbol{x})) = \mathbf{0} & \text{in } \Omega_0 \times (0,T], \quad (2.5)\\ \mathbf{P}(\mathbf{d}, T_a(\mathbf{s}, \boldsymbol{x}))\mathbf{N} = \mathbf{K}^{\text{epi}}\mathbf{d} + \mathbf{C}^{\text{epi}} \dfrac{\partial \mathbf{d}}{\partial t} & \text{on } \Gamma_0^{\text{epi}} \times (0,T], \quad (2.6)\\ \mathbf{P}(\mathbf{d}, T_a(\mathbf{s}, \boldsymbol{x}))\mathbf{N} = -p_{\text{LV}}(t)\, J\mathbf{F}^{-T}\mathbf{N} & \text{on } \Gamma_0^{\text{endo,LV}} \times (0,T], \quad (2.7)\\ \mathbf{P}(\mathbf{d}, T_a(\mathbf{s}, \boldsymbol{x}))\mathbf{N} = -p_{\text{RV}}(t)\, J\mathbf{F}^{-T}\mathbf{N} & \text{on } \Gamma_0^{\text{endo,RV}} \times (0,T], \quad (2.8)\\ \mathbf{P}(\mathbf{d}, T_a(\mathbf{s}, \boldsymbol{x}))\mathbf{N} = |J\mathbf{F}^{-T}\mathbf{N}| \left[p_{\text{LV}}(t)\mathbf{v}_{\text{LV}}^{\text{base}}(\boldsymbol{x}, t) + p_{\text{RV}}(t)\mathbf{v}_{\text{RV}}^{\text{base}}(\boldsymbol{x}, t)\right] & \text{on } \Gamma_0^{\text{base}} \times (0,T], \quad (2.9)\end{cases}$$

$$(\mathscr{C})\quad \frac{d\boldsymbol{c}(t)}{dt} = \boldsymbol{D}(t, \boldsymbol{c}(t), p_{\text{LV}}(t), p_{\text{RV}}(t)) \qquad \text{for } t \in (0,T], \quad (2.10)$$

$$(\mathscr{V})\begin{cases} V_{\text{LV}}^{\text{3D}}(\mathbf{d}(t)) = V_{\text{LV}}(\boldsymbol{c}(t)) & \text{for } t \in (0,T], \quad (2.11)\\ V_{\text{RV}}^{\text{3D}}(\mathbf{d}(t)) = V_{\text{RV}}(\boldsymbol{c}(t)) & \text{for } t \in (0,T]. \quad (2.12)\end{cases}$$

The definition of the vectors $\mathbf{v}_{\text{LV}}^{\text{base}}$ and $\mathbf{v}_{\text{RV}}^{\text{base}}$ appearing in the boundary conditions of the mechanical model $(\mathscr{M})$ and the variables V_{i}^{3D} and V_{i} (with i = LV,RV) of the volume conservation constraints $(\mathscr{V})$ will be provided later in Sections 2.2.3 and 2.2.4, respectively. Finally, the model is closed by the initial conditions in $\Omega_0 \times \{0\}$:

$$u = u_0, \quad \boldsymbol{w} = \boldsymbol{w}_0, \quad \mathbf{s} = \mathbf{s}_0, \quad \mathbf{d} = \mathbf{d}_0, \quad \frac{\partial \mathbf{d}}{\partial t} = \dot{\mathbf{d}}_0, \quad \boldsymbol{c} = \boldsymbol{c}_0.$$

2.2.1. Electrophysiology $(\mathscr{E})$

We model the electric activity in the cardiac tissue by means of problem $(\mathscr{E})$, that is the monodomain equation (2.1) endowed with a suitable ionic model (2.2) for the human ventricular action potential [17,75,77]. In the electrophysiology core model $(\mathscr{E})$, the unknowns are the transmembrane potential u and the ionic variables $\boldsymbol{w}$. The vector $\boldsymbol{w} = \{w_k\}_{k=1}^{n_{\boldsymbol{w}}}$ encodes the gating variables (representing the fraction of open channels per unit area across the cell membrane) and the concentration of specific ionic species. Among them, one variable represents the intracellular calcium concentration $[Ca^{2+}]_i$ (indicated with w_{Ca} in Eq. (2.4)), which plays a key role in the active force generation mechanism. The constant χ_m represents the surface area-to-volume ratio of cardiomyocytes, C_m represents the trans-membrane capacitance per unit area. The applied current $\mathcal{I}_{\text{app}}$ mimics the effect of the Purkinje network [88–90] modeled in this work by means of a surrogate fast endocardial conduction layer [73] represented by $\phi_{\text{fast}} = \phi_{\text{fast}}(\phi) \leq \epsilon$ built as a function of the transmural distance defined in Section 2.1, see also Fig. 1(d). The reaction terms $\mathcal{I}_{\text{ion}}$ and $\boldsymbol{H}$ (specified by the ionic model at hand) couple together the action potential propagation and the cellular dynamics. Specifically, we use the ventricular ten Tusscher–Panfilov ionic model (TTP06, $n_{\boldsymbol{w}} = 18$), which is able to accurately describe ions dynamics across the cell membrane [91]. Furthermore, problem $(\mathscr{E})$ is equipped with homogeneous Neumann boundary conditions (2.3).

The action potential propagation is driven by the diffusion term $\nabla \cdot (J\mathbf{F}^{-1}\boldsymbol{D}\mathbf{F}^{-T}\nabla u)$ where we introduced the deformation gradient tensor $\mathbf{F} = \mathbf{I} + \nabla \mathbf{d}$ with $J = \det(\mathbf{F}) > 0$. The diffusion tensor reads:

$$\boldsymbol{D} = \sigma_\ell(\phi_{\text{fast}}) \frac{\mathbf{f}_0 \otimes \mathbf{f}_0}{\|\mathbf{f}_0\|^2} + \sigma_t(\phi_{\text{fast}}) \frac{\mathbf{s}_0 \otimes \mathbf{s}_0}{\|\mathbf{s}_0\|^2} + \sigma_n(\phi_{\text{fast}}) \frac{\mathbf{n}_0 \otimes \mathbf{n}_0}{\|\mathbf{n}_0\|^2},$$

where $\sigma_\ell(\phi_{\text{fast}})$, $\sigma_t(\phi_{\text{fast}})$, $\sigma_n(\phi_{\text{fast}})$ are the longitudinal, transversal and normal conductivities, respectively, defined as

$$\sigma_k(\phi_{\text{fast}}) = \begin{cases} \sigma_{k,\text{fast}} & \text{if } \phi_{\text{fast}} \leq \epsilon, \quad k = \ell, t, n,\\ \sigma_{k,\text{myo}} & \text{if } \phi_{\text{fast}} > \epsilon, \quad k = \ell, t, n,\end{cases}$$

where $\sigma_{k,\text{fast}}$ and $\sigma_{k,\text{myo}}$ (with $k = \ell, t, n$) are the prescribed conductivities inside and outside the fast endocardial layer, respectively.

2.2.2. Activation ($\mathscr{A}$)

Mechanical activation of cardiac tissue is modeled by means of Eq. (2.4), a system of ODEs standing for an Artificial Neural Network (ANN) based model that surrogates the so called RDQ18 high-fidelity model proposed in [82]. The RDQ18 model [92] is based on a biophysically detailed description of the microscopic active force generation mechanisms taking place at the scale of sarcomeres [81,93]. The RDQ18-ANN model has the great advantage of strikingly reducing the computational burden associated to the numerical solution of the RDQ18 model, yet reproducing its results with a very good accuracy [82].

In the activation core model ($\mathscr{A}$) the unknown is the two-variable state vector $\mathbf{s}$. The input variables in the model are: the scalar field w_{Ca}, denoting the intracellular calcium ions concentration $[\mathrm{Ca}^{2+}]_{\mathrm{i}}$ over the domain Ω_0, provided by the TTP06 ionic model; the scalar field SL, representing the elongation of the sarcomeres belonging to each region of the domain Ω_0, defined as $SL = SL_0\sqrt{\mathcal{I}_{4f}(\mathbf{d})}$, where SL_0 denotes the sarcomere length at rest and $\mathcal{I}_{4f} = \mathbf{F}\mathbf{f}_0 \cdot \mathbf{F}\mathbf{f}_0$ is a measure of the tissue stretch along the fibers direction. This creates a feedback between the mechanical model ($\mathscr{M}$) and the force generation model ($\mathscr{A}$) [15].

The RDQ18-ANN output is the permissivity $P \in [0, 1]$ which is obtained as a function of $\mathbf{s}$: $P = G(\mathbf{s})$ where G is a linear function defined in [82]. Since P is the fraction of the contractile units in the force-generation state, the active tension is given by $T_{\mathrm{a}} = T_{\mathrm{a}}^{\max} P$, where $T_{\mathrm{a}}^{\max}$ denotes the tension generated when all the contractile units are generating force (i.e. for $P = 1$). Finally, to account for a different active tension between LV and RV we define a spatial heterogeneous active tension

$$T_{\mathrm{a}}(\mathbf{s}, \boldsymbol{x}) = T_{\mathrm{a}}^{\max} G(\mathbf{s}) \left[\hat{\xi}(\boldsymbol{x}) + C_{\mathrm{lrv}}(1 - \hat{\xi}(\boldsymbol{x}))\right],$$

where $\hat{\xi} \in [0, 1]$ is the normalized inter-ventricular distance, defined in Section 2.1, and $C_{\mathrm{lrv}} \in (0, 1]$ represents the left–right ventricle contractility ratio.

2.2.3. Mechanics ($\mathscr{M}$)

The mechanical response of the cardiac tissue is described by problem ($\mathscr{M}$) under the hyperelasticity assumption and by adopting an active stress approach [84,85]. The unknown is the displacement $\mathbf{d}$, whereas ρ_{s} is the density. The first Piola–Kirchhoff stress tensor $\mathbf{P} = \mathbf{P}(\mathbf{d}, T_{\mathrm{a}})$ is additively decomposed according to

$$\mathbf{P}(\mathbf{d}, T_{\mathrm{a}}) = \frac{\partial \mathcal{W}(\mathbf{F})}{\partial \mathbf{F}} + T_{\mathrm{a}}(\mathbf{s}, \boldsymbol{x})\left[n_{\mathrm{f}} \frac{\mathbf{F}\mathbf{f}_0 \otimes \mathbf{f}_0}{\sqrt{\mathcal{I}_{4f}}} + n_{\mathrm{s}} \frac{\mathbf{F}\mathbf{s}_0 \otimes \mathbf{s}_0}{\sqrt{\mathcal{I}_{4s}}} + n_{\mathrm{n}} \frac{\mathbf{F}\mathbf{n}_0 \otimes \mathbf{n}_0}{\sqrt{\mathcal{I}_{4n}}}\right], \tag{3}$$

where the first term represents the passive mechanics with $\mathcal{W} : \mathrm{Lin}^+ \to \mathbb{R}$ being the strain energy density function, whereas the second one stands for the orthotropic active stress, with $T_{\mathrm{a}}(\mathbf{s}, \boldsymbol{x})$ the active tension provided by the activation model ($\mathscr{A}$). Moreover, $\mathcal{I}_{4s} = \mathbf{F}\mathbf{s}_0 \cdot \mathbf{F}\mathbf{s}_0$ and $\mathcal{I}_{4n} = \mathbf{F}\mathbf{n}_0 \cdot \mathbf{F}\mathbf{n}_0$ are the tissue stretches along the sheet and sheet-normal directions, respectively, and n_{f}, n_{s} and n_{n} the prescribed proportion of active tension along the fiber, sheet and sheet-normals directions, respectively. Notice that the orthotropic active stress tensor (3) surrogates the contraction caused by dispersed myofibers [31,58,62,63].

To model the passive behavior of the cardiac tissue, we employ the orthotropic Guccione constitutive law [83], according to which the strain energy function is defined as

$$\mathcal{W} = \frac{\kappa}{2}(J - 1)\log(J) + \frac{a}{2}\left(e^{Q} - 1\right),$$

where the first term is the volumetric energy with the bulk modulus κ, which penalizes large variation of volume to enforce a weakly incompressible behavior [94,95], and the exponent Q reads

$$Q = b_{\mathrm{ff}}E_{\mathrm{ff}}^2 + b_{\mathrm{ss}}E_{\mathrm{ss}}^2 + b_{\mathrm{nn}}E_{\mathrm{nn}}^2 + b_{\mathrm{fs}}\left(E_{\mathrm{fs}}^2 + E_{\mathrm{sf}}^2\right) + b_{\mathrm{fn}}\left(E_{\mathrm{fn}}^2 + E_{\mathrm{nf}}^2\right) + b_{\mathrm{sn}}\left(E_{\mathrm{sn}}^2 + E_{\mathrm{ns}}^2\right),$$

where a is the stiffness scaling parameter, $E_{\mathrm{ij}} = \boldsymbol{E}\mathbf{i}_0 \cdot \mathbf{j}_0$, for $\mathrm{i}, \mathrm{j} \in \{\mathrm{f}, \mathrm{s}, \mathrm{n}\}$ and $\mathbf{i}_0, \mathbf{j}_0 \in \{\mathbf{f}_0, \mathbf{s}_0, \mathbf{n}_0\}$, are the entries of $\mathbf{E} = \frac{1}{2}(\mathbf{C} - \mathbf{I})$, i.e the Green–Lagrange strain tensor, being $\mathbf{C} = \mathbf{F}^T\mathbf{F}$ the right Cauchy–Green deformation tensor.

To model the mechanical constraint provided by the pericardium [96–98], we impose at the epicardial boundary Γ_0^{epi} a generalized Robin boundary condition (2.6) by defining the tensors $\mathbf{K}^{\mathrm{epi}} = K_{\parallel}^{\mathrm{epi}}(\mathbf{N} \otimes \mathbf{N} - \mathbf{I}) - K_{\perp}^{\mathrm{epi}}(\mathbf{N} \otimes \mathbf{N})$ and $\mathbf{C}^{\mathrm{epi}} = C_{\parallel}^{\mathrm{epi}}(\mathbf{N} \otimes \mathbf{N} - \mathbf{I}) - C_{\perp}^{\mathrm{epi}}(\mathbf{N} \otimes \mathbf{N})$, where $K_{\perp}^{\mathrm{epi}}$, $K_{\parallel}^{\mathrm{epi}}$, $C_{\perp}^{\mathrm{epi}}$, $C_{\parallel}^{\mathrm{epi}} \in \mathbb{R}^+$ are the stiffness and viscosity parameters of the epicardial tissue in the normal and tangential directions, respectively. Normal stress boundary conditions (2.7)–(2.8) were imposed at the endocardia $\Gamma_0^{\mathrm{endo,LV}}$ and $\Gamma_0^{\mathrm{endo,RV}}$ of both ventricles where $p_{\mathrm{LV}}(t)$ and

$p_{\mathrm{RV}}(t)$ represent the pressure exerted by the blood in the left and right ventricular chambers, respectively. To take into account the effect of the neglected part, over the basal plane, on the biventricular domain, we set on Γ_0^{base} the energy-consistent boundary condition (2.9) in weighted-stress-distribution form, where

$$\mathbf{v}_{\mathrm{LV}}^{\mathrm{base}}(\boldsymbol{x},t)=\hat{\xi}(\boldsymbol{x})\frac{\int_{\Gamma_0^{\mathrm{endo,LV}}} J\mathbf{F}^{-T}\mathbf{N}d\Gamma_0}{\int_{\Gamma_0^{\mathrm{base}}}\hat{\xi}(\boldsymbol{x})\,|J\mathbf{F}^{-T}\mathbf{N}|d\Gamma_0},\qquad \mathbf{v}_{\mathrm{RV}}^{\mathrm{base}}(\boldsymbol{x},t)=(1-\hat{\xi}(\boldsymbol{x}))\frac{\int_{\Gamma_0^{\mathrm{endo,RV}}} J\mathbf{F}^{-T}\mathbf{N}d\Gamma_0}{\int_{\Gamma_0^{\mathrm{base}}}(1-\hat{\xi}(\boldsymbol{x}))\,|J\mathbf{F}^{-T}\mathbf{N}|d\Gamma_0}. \tag{4}$$

The energy-consistent boundary condition considered in this work is the extension to the biventricular case of the energy-consistent boundary condition originally proposed in [82] for LV. The complete derivation can be found in Appendix B. The name of this boundary condition is motivated by the resulting formulation of the 3D–0D coupled cardiovascular model, which is compliant with the principle of energy conservation, as demonstrated in [82]. In contrast, unless accurate imaging measures of basal displacement were available, the conservation of energy would not be guaranteed if, e.g., Neumann or Dirichlet boundary conditions are prescribed at the ventricular base [82].

2.2.4. Blood circulation ($\mathscr{C}$) and coupling conditions ($\mathscr{V}$)

We model the blood circulation through the entire cardiovascular system (i.e. Eq. (2.10)) by means of a closed-loop model, inspired by [25,42] and recently proposed in [15]. In the 0D closed-loop model, systemic and pulmonary circulations are modeled with RLC circuits, heart chambers are described by time-varying elastance elements and non-ideal diodes stand for the heart valves [15].

The circulation core model ($\mathscr{C}$) is represented by a system of ODEs expressed by Eq. (2.10), where $\boldsymbol{D}$ is a proper function (defined in [15]) and $\boldsymbol{c}(t)$ includes pressures, volumes and fluxes of the different compartments composing the vascular network:

$$\begin{aligned}\boldsymbol{c}(t)=&(V_{\mathrm{LA}}(t),\,V_{\mathrm{LV}}(t),\,V_{\mathrm{RA}}(t),\,V_{\mathrm{RV}}(t),\,p_{\mathrm{AR}}^{\mathrm{SYS}}(t),\,p_{\mathrm{VEN}}^{\mathrm{SYS}}(t),\,p_{\mathrm{AR}}^{\mathrm{PUL}}(t),\,p_{\mathrm{VEN}}^{\mathrm{PUL}}(t),\\ &Q_{\mathrm{AR}}^{\mathrm{SYS}}(t),\,Q_{\mathrm{VEN}}^{\mathrm{SYS}}(t),\,Q_{\mathrm{AR}}^{\mathrm{PUL}}(t),\,Q_{\mathrm{VEN}}^{\mathrm{PUL}}(t))^{T}.\end{aligned}$$

Here V_{LA}, V_{RA}, V_{LV} and V_{RV} refer to the volumes of left atrium, right atrium, LV and RV, respectively; $p_{\mathrm{AR}}^{\mathrm{SYS}}$, $Q_{\mathrm{AR}}^{\mathrm{SYS}}$, $p_{\mathrm{VEN}}^{\mathrm{SYS}}$, $Q_{\mathrm{VEN}}^{\mathrm{SYS}}$, $p_{\mathrm{AR}}^{\mathrm{PUL}}$, $Q_{\mathrm{AR}}^{\mathrm{PUL}}$, $p_{\mathrm{VEN}}^{\mathrm{PUL}}$ and $Q_{\mathrm{VEN}}^{\mathrm{PUL}}$ express pressures and flow rates of the systemic and pulmonary circulation (arterial and venous). For the complete mathematical description of the 0D circulation lumped model we refer to [15].

To couple the 0D circulation model ($\mathscr{C}$) with the 3D biventricular model, given by ($\mathscr{E}$)–($\mathscr{A}$)–($\mathscr{M}$), we follow the strategy proposed in [15]: we replace the time-varying elastance elements representing LV and RV in the circulation model with its corresponding 3D electromechanical description, obtaining the coupled 3D–0D model depicted in Fig. 2. With this aim, we introduce the volume-consistency coupling conditions ($\mathscr{V}$) where

$$V_{\mathrm{i}}^{\mathrm{3D}}(\mathbf{d}(t))=\int_{\Gamma_0^{\mathrm{endo,i}}} J(t)\,((\mathbf{h}\otimes\mathbf{h})\,(\mathbf{x}+\mathbf{d}(t)-\mathbf{b}_{\mathrm{i}}))\cdot\mathbf{F}^{-T}(t)\mathbf{N}\,d\Gamma_0\qquad \mathrm{i}=\mathrm{LV},\mathrm{RV}$$

wherein $\mathbf{h}$ is a vector orthogonal to LV/RV centerline (i.e. lying on the biventricular base) and $\mathbf{b}_{\mathrm{i}}$ lays inside LV/RV [15].

In virtue of the volumetric condition ($\mathscr{V}$), $p_{\mathrm{LV}}(t)$ and $p_{\mathrm{RV}}(t)$ act as Lagrange multipliers in the 3D–0D coupled model (2). Indeed, their values are determined by means of the coupling between blood circulation ($\mathscr{C}$) and tissue mechanics ($\mathscr{M}$).

2.3. Reference configuration and initial tissue displacement

Cardiac geometries are acquired from in vivo medical images through imaging techniques. These geometries are in principle not stress free, due to the blood pressure acting on the endocardia. Therefore, we need to estimate the unloaded (i.e. stress-free) configuration (also named *reference configuration*) to which the 3D–0D model (2) refers. To recover the reference configuration Ω_0, starting from a geometry $\widetilde{\Omega}$ acquired from medical images (typically during the diastolic phase), we extend to the biventricular case the procedure proposed for LV in [15].

We assume that the configuration $\widetilde{\Omega}$ is acquired during the diastole, when the biventricular geometry is loaded with $p_{\mathrm{LV}}=\widetilde{p}_{\mathrm{LV}}$, $p_{\mathrm{RV}}=\widetilde{p}_{\mathrm{RV}}$ and a residual active tension $T_{\mathrm{a}}=\widetilde{T}_{\mathrm{a}}>0$ is present. To recover the reference

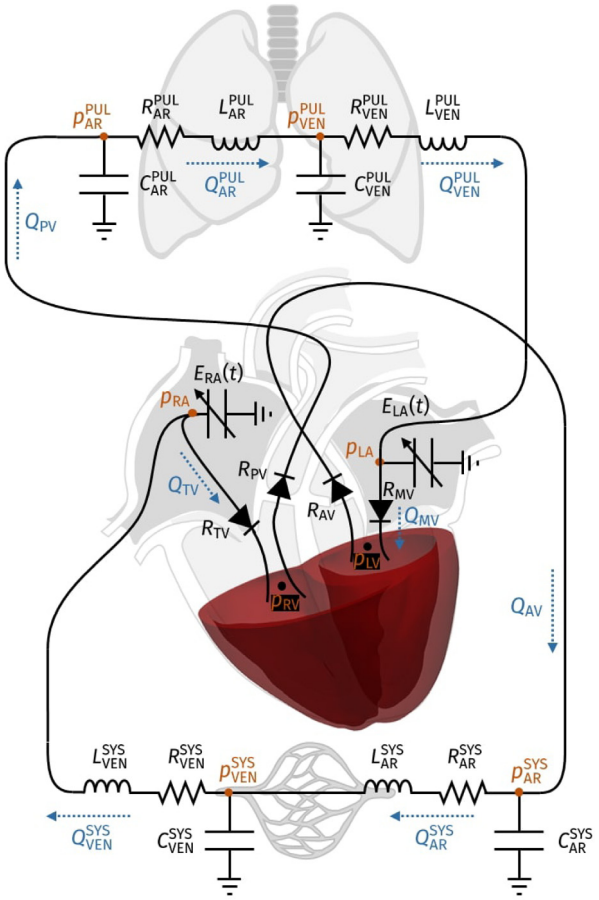

Fig. 2. 3D–0D coupling between the biventricular 3D EM model and the 0D circulation model. The state variables corresponding to pressures and fluxes are depicted in orange and blue, respectively. (For interpretation of the references to color in this figure legend, the reader is referred to the web version of this article.)

configuration Ω_0 we solve the following inverse problem: find the domain Ω_0 such that, if we inflate Ω_0 by $\mathbf{d}$, solution of the differential problem[1]

$$\begin{cases} \nabla \cdot \mathbf{P}(\mathbf{d}, T_a) = \mathbf{0} & \text{in } \Omega_0, \\ \mathbf{P}(\mathbf{d}, T_a)\mathbf{N} + \mathbf{K}^{epi}\mathbf{d} = \mathbf{0} & \text{on } \Gamma_0^{epi}, \\ \mathbf{P}(\mathbf{d}, T_a)\mathbf{N} = -p_{LV}\, J\mathbf{F}^{-T}\mathbf{N} & \text{on } \Gamma_0^{endo,LV}, \\ \mathbf{P}(\mathbf{d}, T_a)\mathbf{N} = -p_{RV}\, J\mathbf{F}^{-T}\mathbf{N} & \text{on } \Gamma_0^{endo,RV}, \\ \mathbf{P}(\mathbf{d}, T_a)\mathbf{N} = |J\mathbf{F}^{-T}\mathbf{N}| \left[p_{LV}\mathbf{v}_{LV}^{base}(\boldsymbol{x}) + p_{RV}\mathbf{v}_{RV}^{base}(\boldsymbol{x}) \right] & \text{on } \Gamma_0^{base}, \end{cases} \tag{5}$$

obtained for $p_{LV} = \widetilde{p}_{LV}$, $p_{RV} = \widetilde{p}_{RV}$ and $T_a = \widetilde{T}_a$, we get the domain $\widetilde{\Omega}$.

After recovering Ω_0, we inflate the biventricular reference configuration Ω_0 by solving again problem (5), where we set the pressures $p_{LV} = p_{LV}^{ED}$ and $p_{RV} = p_{RV}^{ED}$ with the superscript ED stands for the end-diastolic phase. The values p_{LV}^{ED} and p_{RV}^{ED} are chosen to bring the biventricular domain to defined end diastolic volumes for the left V_{LV}^{ED} and right V_{RV}^{ED} ventricles. In this way we obtain the end-diastolic configuration for the biventricular geometry. Hence, the solution $\mathbf{d}$ of the problem (5) is set as initial condition $\mathbf{d}_0$ for $\mathbf{d}$ in ($\mathscr{M}$). The above procedure is represented in step 4 of Fig. 4.

[1] The problem (5) is derived from ($\mathscr{M}$) setting aside the time dependent terms.

3. Numerical approximation

In this section we illustrate the numerical discretization of the different core models composing the 3D–0D problem (2) along with the strategy that we adopt to reach a limit-cycle.

3.1. Space and time discretizations

For the numerical approximation of the 3D–0D coupled model (2) we follow the approach proposed in [46], which is extended here to the biventricular case. The core models $(\mathscr{E})-(\mathscr{A})-(\mathscr{M})-(\mathscr{C})$ are solved sequentially in a segregated manner by using different resolutions in space and time, to properly handle the different space and time scales of the core models contributing to both cardiac EM and blood circulation [5,55,99]. For this reason we call this numerical approach Segregated-Intergrid-Staggered (SIS).

For the space discretization, we use the Finite Element Method (FEM) with continuous Finite Elements (FEs) of order 1 ($\mathbb{Q}_1$) and hexahedral meshes [100]. We consider two nested meshes $\mathcal{T}_{h_1}$ and $\mathcal{T}_{h_2}$ of the computational domain Ω_0 (h_1 and h_2, with $h_1 < h_2$, represent the mesh sizes), where $\mathcal{T}_{h_1}$ is built by uniformly refining $\mathcal{T}_{h_2}$ [101,102], see Fig. 3(a). We adopt the finer mesh $\mathcal{T}_{h_1}$ for $(\mathscr{E})$, where it is essential to accurately capture the dynamics of traveling waves, while the coarser one ($\mathcal{T}_{h_2}$) is used for both $(\mathscr{A})$ and $(\mathscr{M})$ [2,46,76]. We employ an efficient intergrid transfer operator between the nested grids $\mathcal{T}_{h_1}$ and $\mathcal{T}_{h_2}$, which allows to evaluate the feedback between $(\mathscr{E})$ and $(\mathscr{M})-(\mathscr{A})$ [46]. In [46], the displacement field $\mathbf{d}$ is interpolated on $\mathcal{T}_{h_1}$ and $\nabla\mathbf{d}$ is assembled on the fine mesh directly. Here, we follow the more effective strategy proposed in [16], where $\nabla\mathbf{d}$ is recovered on $\mathcal{T}_{h_2}$ thanks to an L^2 projection [101]. Then, $\nabla\mathbf{d}$ is interpolated on $\mathcal{T}_{h_1}$.

For the time discretization, we use Finite Difference schemes [103]. The cardiac electrophysiology model is solved by means of the Backward Differentiation Formula of order 2 (BDF2). We adopt an implicit–explicit (IMEX) scheme, denoted by $(\mathscr{E}_{\text{IMEX}})$, where the diffusion term is treated implicitly, whereas the ionic and reaction terms explicitly [46,104]. For both mechanical activation and passive mechanics we employ the BDF1 scheme, where $(\mathscr{A}_{\text{E}})$ is advanced in time with an explicit method, whereas a fully implicit scheme is used for $(\mathscr{M}_{\text{I}})-(\mathscr{V}_{\text{I}})$ [46]. Finally, we employ an explicit 4th order Runge–Kutta method (RK4) for $(\mathscr{C}_{\text{E}})$ [46].

We use two different time steps, Δt for $(\mathscr{A}_{\text{E}})-(\mathscr{M}_{\text{I}})-(\mathscr{V}_{\text{I}})-(\mathscr{C}_{\text{E}})$ and $\tau = \Delta t/N_{\text{sub}}$ for $(\mathscr{E}_{\text{IMEX}})$, with $N_{\text{sub}} \in \mathbb{N}$, see Fig. 3(c). We first update the variables of $(\mathscr{E}_{\text{IMEX}})$, then those of $(\mathscr{A}_{\text{E}})$ and finally, after updating the unknowns of $(\mathscr{M}_{\text{I}})-(\mathscr{V}_{\text{I}})$, we update the ones of $(\mathscr{C}_{\text{E}})$, see Fig. 3(b).

The whole algorithm for the SIS numerical scheme is reported in Fig. 3.

3.2. 3D–0D coupled problem resolution

We couple the 3D mechanical model $(\mathscr{M})$ with the 0D closed-loop hemodynamic model $(\mathscr{C})$ by means of the volume conservation constraints $(\mathscr{V})$, where the pressures of LV and RV act as Lagrange multipliers [46]. In Fig. 3(b) (steps 3–4) we obtain a saddle point problem $(\mathscr{M}_{\text{I}})-(\mathscr{V}_{\text{I}})$.

We introduce the discrete times $t^n = n\Delta t$, $n \geq 0$ and we denote by $\mathbf{a}_{\text{h}}^n \simeq \mathbf{a}_{\text{h}}(t^n)$ the fully discretized FEM approximation of the generic (scalar, vectorial or tensorial) variable $\mathbf{a}(t)$ (i.e. the vector collecting the degrees of freedom, DOFs, defined over the computational mesh $\mathcal{T}_{h_2}$ at time t^n). Then, at each time step t^{n+1}, the fully discretized version of $(\mathscr{M}_{\text{I}})-(\mathscr{V}_{\text{I}})$ reads:

$$
\begin{cases}
\left(\rho_s \dfrac{1}{(\Delta t)^2}\mathcal{M} + \dfrac{1}{\Delta t}\mathcal{F} + \mathcal{G}\right)\mathbf{d}_{\text{h}}^{n+1} + \boldsymbol{S}(\mathbf{d}_{\text{h}}^{n+1}, T_{\text{a,h}}^{n+1}) \\
\qquad = \rho_s \dfrac{2}{(\Delta t)^2}\mathcal{M}\mathbf{d}_{\text{h}}^{n} - \rho_s \dfrac{1}{(\Delta t)^2}\mathcal{M}\mathbf{d}_{\text{h}}^{n-1} + \dfrac{1}{\Delta t}\mathcal{F}\mathbf{d}_{\text{h}}^{n} \\
\qquad + p_{\text{LV}}^{n+1}\boldsymbol{P}_{\text{LV}}(\mathbf{d}_{\text{h}}^{n}, \mathbf{d}_{\text{h}}^{n+1}) + p_{\text{RV}}^{n+1}\boldsymbol{P}_{\text{RV}}(\mathbf{d}_{\text{h}}^{n}, \mathbf{d}_{\text{h}}^{n+1}) \\
V_{\text{LV}}^{\text{3D}}(\mathbf{d}_{\text{h}}^{n+1}) = V_{\text{LV}}(\boldsymbol{c}^n) \\
V_{\text{RV}}^{\text{3D}}(\mathbf{d}_{\text{h}}^{n+1}) = V_{\text{RV}}(\boldsymbol{c}^n)
\end{cases}
\tag{6}
$$

where we introduced

$$
\mathcal{M}_{\text{ij}} = \int_{\Omega_0} \boldsymbol{\phi}_{\text{j}} \cdot \boldsymbol{\phi}_{\text{i}}\, d\Omega_0, \qquad \boldsymbol{S}_{\text{i}} = \int_{\Omega_0} \mathbf{P}(\mathbf{d}_{\text{h}}^{n+1}, T_{\text{a,h}}^{n+1}) : \nabla\boldsymbol{\phi}_{\text{i}}\, d\Omega_0,
$$

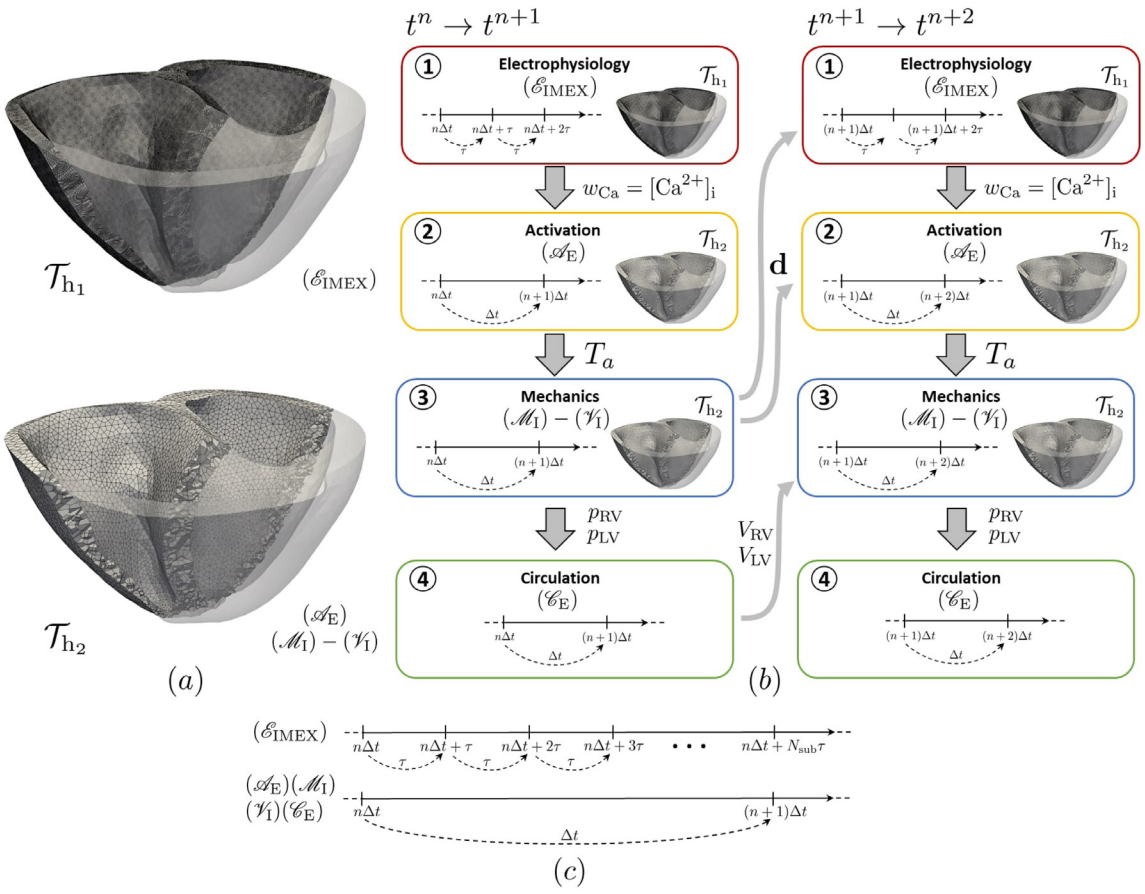

Fig. 3. Segregated-intergrid-staggered numerical scheme: (a) nested meshes $\mathcal{T}_{h_1}$ and $\mathcal{T}_{h_2}$ (with $h_1 < h_2$); (b) schematic representation of the numerical scheme; (c) graphical representation of the time advancement scheme.

$$
\begin{aligned}
\mathcal{F}_{ij} &= \int_{\Gamma_0^{\text{epi}}} \left[C_{\parallel}^{\text{epi}}(\mathbf{N}_h \otimes \mathbf{N}_h - \mathbf{I}_h) - C_{\perp}^{\text{epi}}(\mathbf{N}_h \otimes \mathbf{N}_h) \right] \boldsymbol{\phi}_j \cdot \boldsymbol{\phi}_i \, d\Gamma_0, \\
\mathcal{G}_{ij} &= \int_{\Gamma_0^{\text{epi}}} \left[K_{\parallel}^{\text{epi}}(\mathbf{N}_h \otimes \mathbf{N}_h - \mathbf{I}_h) - K_{\perp}^{\text{epi}}(\mathbf{N}_h \otimes \mathbf{N}_h) \right] \boldsymbol{\phi}_j \cdot \boldsymbol{\phi}_i \, d\Gamma_0, \\
\boldsymbol{P}_{k,i} &= \int_{\Gamma_0^{\text{base}}} |J_h^{n+1}(\mathbf{F}_h^{n+1})^{-T}\mathbf{N}_h| \mathbf{v}_{k,h}^{\text{base,n}} \cdot \boldsymbol{\phi}_i \, d\Gamma_0 \\
&\quad - \int_{\Gamma_0^{\text{endo,k}}} J_h^{n+1}(\mathbf{F}_h^{n+1})^{-T}\mathbf{N}_h \cdot \boldsymbol{\phi}_i \, d\Gamma_0, \qquad \text{k=LV, RV.}
\end{aligned}
$$

Here $\mathbf{F}_h^{n+1} = \mathbf{I}_h + \nabla \mathbf{d}_h^{n+1}$ with $J_h^{n+1} = \det(\mathbf{F}_h^{n+1})$, $\{\boldsymbol{\phi}_i\}_{i=1}^{N_d}$ represents the set of basis functions for the finite dimensional space $[\mathcal{X}_h^s]^3$ with $\mathcal{X}_h^s = \{v \in C^0(\bar{\Omega}_0) : v|_K \in \mathbb{Q}_s(K), \, s \geq 1, \quad \forall K \in \mathcal{T}_{h_2}\}$, where $\mathbb{Q}_s(K)$ stands for the set of polynomials with degree smaller than or equal to s over a mesh element K and $N_{\mathbf{d}} = \dim([\mathcal{X}_h^s]^3)$ is the numbers of DOFs for the displacement.

Moving all the terms to the right hand side, Eq. (6) can be compactly written as:

$$
\begin{cases}
\mathbf{r}_{\mathbf{d}}(\mathbf{d}_h^{n+1}, p_{\text{LV}}^{n+1}, p_{\text{RV}}^{n+1}) & = \mathbf{0} \\
r_{p_{\text{LV}}}(\mathbf{d}_h^{n+1}) & = 0 \\
r_{p_{\text{RV}}}(\mathbf{d}_h^{n+1}) & = 0
\end{cases} \tag{7}
$$

for suitable functions $r_{p_{\text{LV}}}$, $r_{p_{\text{RV}}}$ and $\mathbf{r}_{\mathbf{d}}$.

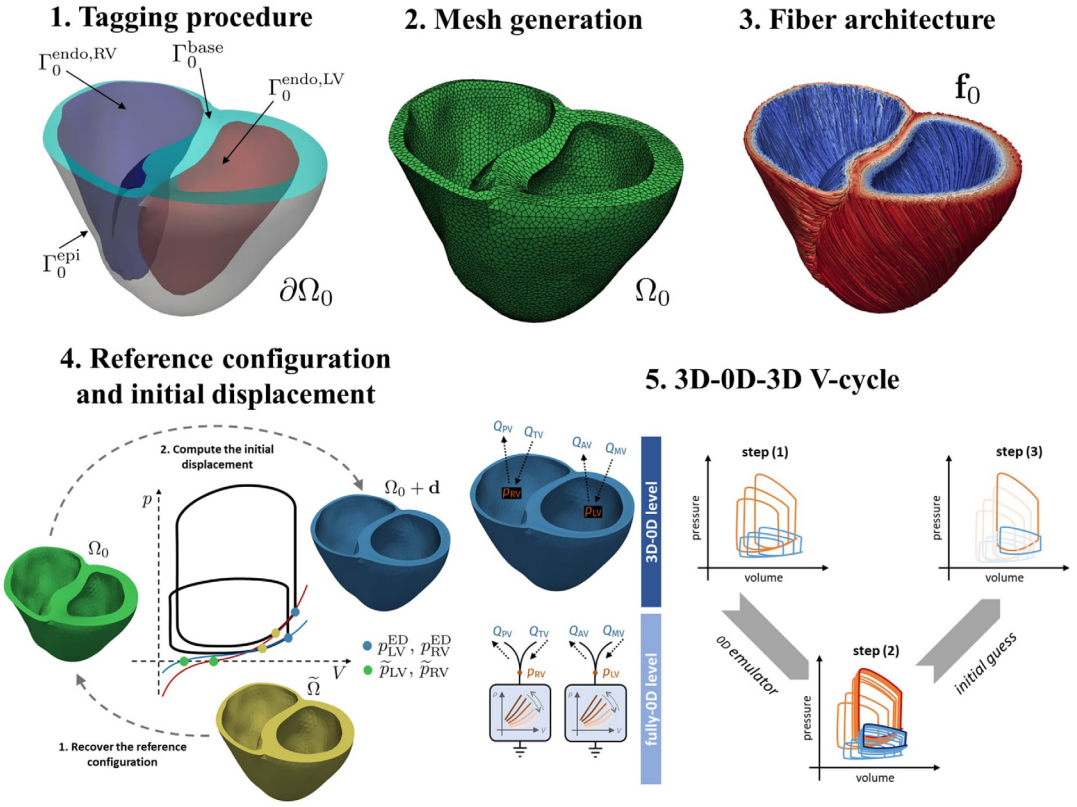

Fig. 4. Graphical display of the whole pipeline for the initialization of a numerical simulation employing the 3D–0D EM model.

We solve the non-linear saddle-point problem (7) by means of the Newton algorithm using, at the algebraic level, the Schur complement reduction [105]. More details about the solution of the problem (7) can be found in Appendix C.

3.3. Finding initial conditions for the multiphysics problem

The numerical results of the 3D–0D EM model typically feature a temporal transient, which lasts for several heartbeats and converges to a periodic solution, known as *limit cycle*. The outputs of clinical interest should be computed from the numerical solution that is associated with the limit cycle. To reduce the computational overhead of reaching a periodic solution, we follow the strategy proposed in [106], aimed at accelerating the convergence towards the limit cycle. This strategy – named 3D–0D-3D V-cycle – comprises three stages (see point 5 of Fig. 4). In a first step, three heartbeats are simulated with the 3D–0D model. Then, based on the PV-loops obtained from the previous 3D–0D model, a 0D emulator of each ventricle is built with the aim of surrogating the pressure–volume relationships, and substituted to the 3D model. These emulators, coupled with the 0D model of blood circulation for the remaining compartments, allow to simulate the transient phase towards a periodic solution in less than one minute of computational time on a standard laptop. Finally, the state obtained with this fully 0D model is used to initialize the 3D–0D model, and three additional heartbeats are simulated. Overall, the computational cost of reaching the limit cycle amounts to that of simulating six heartbeats, regardless of the number of cycles required to converge to a periodic solution. As a matter of fact, the computational time required by the 0D surrogate model is negligible compared to that of the full-order 3D–0D model. More details on this pipeline are available in [106].

To find an initial guess for the remaining variables, we initialize the ionic model by running a 1000-cycle long single-cell simulation. Similarly, we initialize the force generation model by means of a single-cell simulation with

Table 1
Number of nodes and DOFs for the two nested meshes $\mathcal{T}_{h_1}$ and $\mathcal{T}_{h_2}$ employed for ($\mathscr{E}$) and ($\mathscr{A}$)-($\mathscr{M}$) by using FEs of order 1 ($\mathbb{Q}_1$).

Mesh	Physics	Number of nodes	DOFs
$\mathcal{T}_{h_1}$	($\mathscr{E}$)	4'290'929	4'290'929
$\mathcal{T}_{h_2}$	($\mathscr{A}$)	78'491	78'491
$\mathcal{T}_{h_2}$	($\mathscr{M}$)	78'491	235'473

a constant calcium input (corresponding to the final calcium concentration of the single-cell ionic simulation) and a reference sarcomere length $SL = 2.2\,\mu m$.

The whole pipeline for the initialization of a numerical simulation employing the 3D–0D biventricular EM model is sketched in Fig. 4.

4. Numerical results

In this section, we present several biventricular electromechanical simulations that employ the 3D–0D model discussed in Sections 2 and 3.

We organize this section as follows. After a brief description regarding the setting of the numerical simulations (Section 4.1), we compare the results of a physiological electromechanical simulation with a comprehensive set of experimental data available in the literature (Section 4.2). Then, in Section 4.3 we investigate how different cross-fibers active contraction arrangements affect the electromechanical simulations, by setting different combinations of n_f, n_s and n_n, i.e. of the prescribed proportion of active tension along the myofibers. Finally, in Section 4.4 we evaluate the impact of different myofiber architectures, obtained by three types of LDRBMs, on the biventricular pumping function.

4.1. Setting of numerical simulations

All the simulations are performed on a realistic biventricular geometry processed from the Zygote 3D heart [107], a CAD-model representing an average healthy human heart reconstructed from high-resolution computer tomography scan. To build the computational mesh associated with the biventricular Zygote model, we use the Vascular Modeling Toolkit software [108] (http://www.vmtk.org) by exploiting the semi-automatic meshing tool recently proposed in [109]. In particular, the mesh generation process starts with a tetrahedral volumetric mesh, which is then converted to an hexahedral one, obtained by subdividing each tetrahedron into four hexahedra with the *tet-hex* algorithm [109]; see Fig. 3(a).

We employ two nested meshes where for the activation and the mechanical problems we adopt a mesh size $h_1 = 3\,mm$, while for the electrophysiology problem we employ a mesh size h_2 that is four time smaller [46]. As for the time steps, we use $\tau = 50\ \mu s$ for the electrophysiology problem and $\Delta t = 500\ \mu s$ for the mechanical, activation and circulation problems [46,47]. Table 1 denotes the number of nodes of the electrical ($\mathcal{T}_{h_1}$) and the mechanical ($\mathcal{T}_{h_2}$) meshes, along with the number of DOFs.

The parameters used for the 3D–0D model are listed in Tables 8 and 9 (see Appendix A). The settings related to LDRBMs, adopted for prescribing the fiber architectures, will be specified for each case reported in Sections 4.2–4.4. Table 2 reports the setting used for the non-linear and linear solvers (with preconditioners used to solve the linear systems), respectively.

To approach the limit cycle, we initialize all the numerical simulations, for the coupled 3D–0D model, following the procedure illustrated in Section 3.3 (see also [106]). Then, we perform three further heartbeats using the fully framework of the 3D–0D model presented in Sections 2 and 3. We neglected the first two, so that all the reported results refer to the last heartbeat.

In all the simulations we adopted the same pacing protocol in which five ventricular endocardial areas are activated with spherical impulses: in the anterior para-septal wall, in the left surface of inter-ventricular septum and in the bottom of postero-basal area, for LV; in the septum and in the free endocardial wall, for RV [47,110], see also Fig. 5(c). This, combined with the fast endocardial conduction layer (see Section 2.2.1), surrogates the action of the Purkinje network [73,88].

Table 2
Tolerances of the linear and non-linear solvers for the different core models.

Physics	Linear solver			Non-linear solver		
	Type	Precond.	Abs. tol.	Type	Rel. tol.	Abs. tol.
Fibers	GMRES	AMG	10^{-10}	-	-	-
Monodomain	CG	AMG	10^{-10}	-	-	-
Activation	GMRES	AMG	10^{-10}	-	-	-
Mechanics	GMRES	AMG	10^{-10}	Newton	10^{-10}	10^{-8}
Reference config.	GMRES	AMG	10^{-8}	Newton	10^{-8}	10^{-6}

Table 3
CPU times required to perform an electromechanical simulation of a single heartbeat.

Physics	Time (s)	Percentage (%)
($\mathscr{E}$)	28116	92.630
($\mathscr{A}$)	50	0.165
($\mathscr{M}$)	2186	7.202
($\mathscr{C}$)	1	0.003

The numerical methods presented in Section 3 have been implemented within `life`$^{\mathtt{x}}$ (https://lifex.gitlab.io/lifex), a new in-house high-performance `C++` FE library, for cardiac applications, based on the `deal.II` FE core [111] (https://www.dealii.org). All the numerical simulations were executed using either the `iHeart` cluster (Lenovo SR950 192-Core Intel Xeon Platinum 8160, 2100 MHz and 1.7 TB RAM) at MOX, Dipartimento di Matematica, Politecnico di Milano or the `GALILEO` supercomputer at Cineca (8 nodes endowed with 36 Intel Xeon E5-2697 v4 2.30 GHz). In Table 3 we show the computational times for assembling, preconditioning and solving the different core models. The total CPU time required to perform an electromechanical simulation of one heartbeat with 288 cores on the `GALILEO` supercomputer is about 8 h. The most computationally demanding part of the solver, which accounts for about 93% of the total CPU time, is associated to the ($\mathscr{E}$) core model. This is motivated by the detailed space–time resolution used to approximate the monodomain model.

4.2. Baseline simulation

We present a human electromechanical simulation in physiological conditions related to the Zygote biventricular geometry. For the fibers generation we adopted D-RBM [47,54]. The input angle values (see Section 2.1) were chosen according to observations based on histological studies in the human heart [112,113]:

$$\begin{aligned} &\alpha_{epi,\mathrm{LV}} = -60^\circ, \quad \alpha_{endo,\mathrm{LV}} = +60^\circ, \quad \alpha_{epi,\mathrm{RV}} = -25^\circ, \quad \alpha_{endo,\mathrm{RV}} = +90^\circ; \\ &\beta_{epi,\mathrm{LV}} = +20^\circ, \quad \beta_{endo,\mathrm{LV}} = -20^\circ, \quad \beta_{epi,\mathrm{RV}} = +20^\circ, \quad \beta_{endo,\mathrm{RV}} = 0^\circ. \end{aligned} \tag{8}$$

Moreover, to surrogate the effect of dispersed myofibers, we set in (3) $n_\mathrm{f} = 0.7$, $n_\mathrm{s} = 0$ and $n_\mathrm{n} = 0.3$ for the proportion of active tension along the fiber, sheet and normal directions, respectively [31,59].

Fig. 5 illustrates the time evolution of calcium ions concentration (a), the mechanical deformation (b, e), the activation times (c), the PV-loop curves for both ventricles and the time evolution of pressures and volumes of the four chambers (d). Specifically, in Fig. 5(a) we display the time evolution of the TTP06 ionic model calcium transient showing the physiological wave propagation up to the complete depolarization of both ventricles ($t = 0.12$ s). In Fig. 5(b) we report different snapshots of the biventricular geometry warped by the displacement vector. As expected, at the beginning of the contraction the volumes of both ventricles remain nearly constant while the pressure increases ($t = 0.0 - 0.10$ s); during the ejection phase, the ventricular contraction is clearly visible, with the basal plane that moves towards the bottom while the apex remains almost fixed. Moreover, a significant thickening of the myocardium wall takes place ($t = 0.35$ s). Then, the ventricles start to relax. This leads to a slow recovery of the initial volumes ($t = 0.45 - 0.60$ s). Finally, in Fig. 5(c) we display the simulated activation map in which both the total activation time (120 ms) and the activation pattern are in accordance with the literature [47,110].

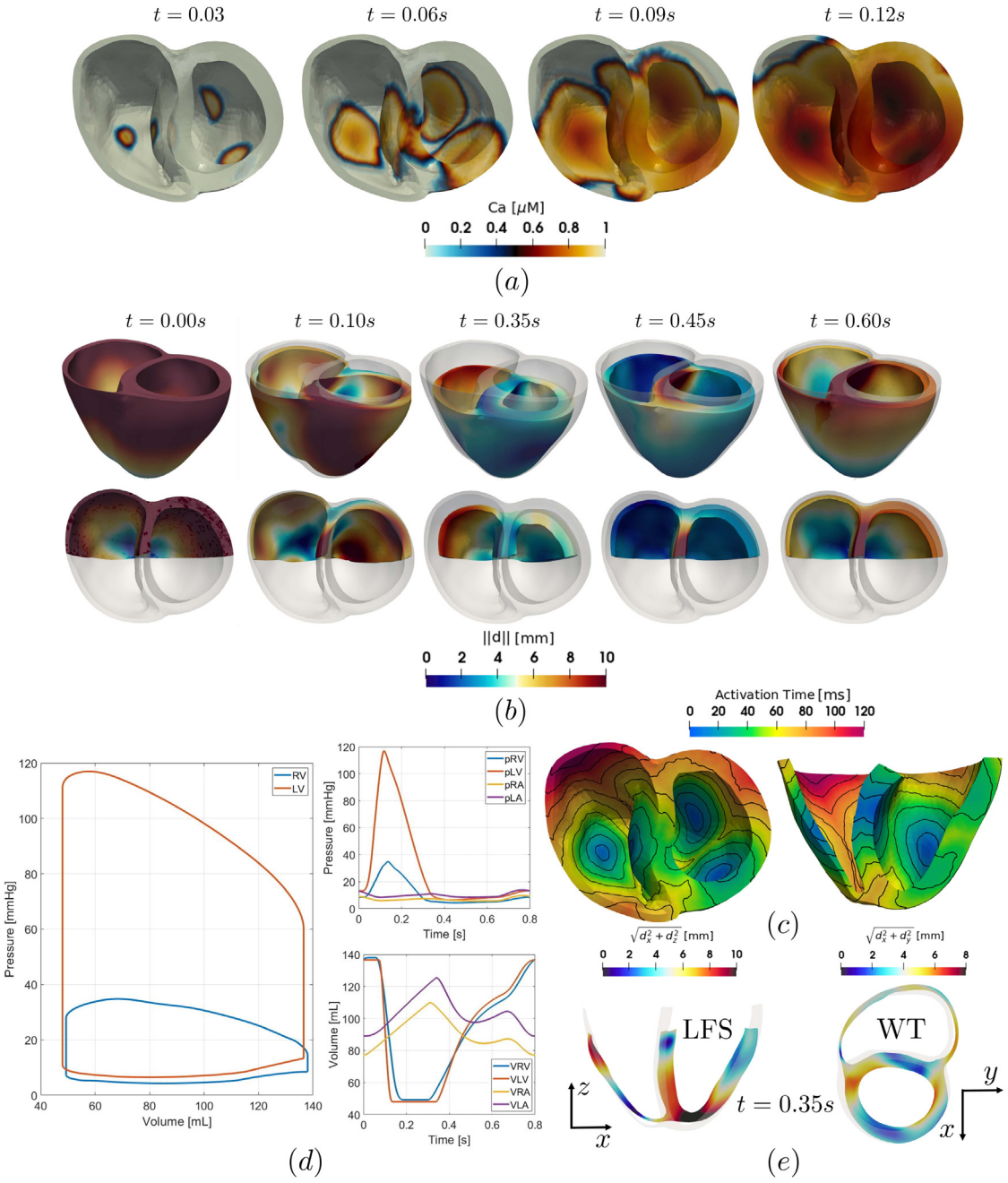

Fig. 5. Baseline EM simulation; (a) calcium transient at four time instants in the cardiac cycle; (b) mechanical displacement magnitude (with respect to the reference configuration) at five time instants of the heartbeat where 0.35 s is the end of systole. (c) activation map; (d, left) PV-loop LV (orange) and RV (blue); (d, right) pressures (top) and volumes (bottom) transient during the cardiac cycle for the four chambers; (e) mid ventricular slices at the end of systole, showing LFS on the left and WT on the right, colored by the in-plane displacement magnitude (i.e $\sqrt{d_x^2 + d_z^2}$ for LFS and $\sqrt{d_x^2 + d_y^2}$ for WT). (For interpretation of the references to color in this figure legend, the reader is referred to the web version of this article.)

In Table 4 we compare some relevant mechanical biomarkers obtained by our numerical simulation with those provided by the data reported in the literature [66–72]. Notice that all the values in Table 4, related to the ventricular volumes, are expressed with absolute values, in mL, estimated for an adult subject, as reported in the quoted

Table 4
Comparison between the simulation results, employing the 3D–0D EM model, and the literature values of mechanical biomarkers in physiological conditions (references are reported in the Table, see also [17,32]).

Mechanical biomarkers	Literature values	Simulation results	Description
EDV_{LV} (mL)	142 ± 21 [66]	137	Left end diastolic volume
EDV_{RV} (mL)	144 ± 23 [68]	138	Right end diastolic volume
ESV_{LV} (mL)	47 ± 10 [66]	48	Left end systolic volume
ESV_{RV} (mL)	50 ± 14 [68]	49	Right end systolic volume
EF_{LV} (%)	67 ± 5 [66]	66	Left ventricular ejection fraction
EF_{RV} (%)	67 ± 8 [67]	65	Right ventricular ejection fraction
P_{LV} (mmHg)	119 ± 13 [69]	117	Left systolic pressure peak
P_{RV} (mmHg)	35 ± 11 [70]	35	Right systolic pressure peak
LFS (%)	13-21 [71]	21	Longitudinal fractional shortening
WT (%)	18-100 [72]	41	Fractional wall thickening

references. However, we are aware that in the clinical practice the ventricular volumes are always indicated as "indexed ventricular volumes", by dividing the ventricular volume for the Body Surface Area of the related patient. The chosen mechanical biomarkers were: (i) left and right end diastolic/systolic volumes (EDV_{LV}, EDV_{RV}, ESV_{LV}, ESV_{RV}), representing the maximal and minimal left and right ventricular volumes achieved during the heartbeat, computed as the maximal (EDV_{LV}, EDV_{RV}) and minimal (ESV_{LV}, ESV_{RV}) volumes in the PV-loop curves, see Fig. 5(d); (ii) left and right ventricular ejection fractions (EF_{LV}, EF_{RV}), which represent the amount of blood that is pumped by LV and RV during a cardiac cycle, computed as

$$EF_i(\%) = \frac{EDV_i - ESV_i}{EDV_i} 100 \qquad i = LV,RV;$$

(iii) left and right systolic pressure peaks (P_{LV}, P_{RV}), the maximal pressures reached in LV and RV, computed as the maximal pressures in the PV-loop curves, see Fig. 5(d); (iv) the systolic longitudinal fractional shortening (LFS), standing for the fractional displacement between the endocardial apex and the base [17], evaluated as

$$LFS(\%) = \frac{L_0 - L}{L_0} 100,$$

where L_0 and L are the apico-basal distance measured at the beginning ($t = 0.0$ s) and at the end of systole ($t = 0.35$ s), see Fig. 5(e); (v) the systolic wall thickening (WT), representing the fractional cardiac wall thickening [17], measured as

$$WT(\%) = \frac{T - T_0}{T} 100,$$

where T_0 and T are the cardiac wall thickening at the beginning ($t = 0.0$ s) and at the end of systole ($t = 0.35$ s), see Fig. 5(e).

All the above mechanical biomarkers, obtained by our numerical simulation, fall within the physiological range (references in Table 4).

4.3. Cross-fibers active contraction

To surrogate the dispersion effect in the cardiac fibers, we analyze several cross-fibers active contraction arrangements, by setting in Eq. (3) different combinations of n_f, n_s and n_n, i.e. the prescribed proportion of active tension along the myofibers. Five different sets were chosen: (i) $n_f = 0.7$, $n_s = 0.3$, $n_n = 0$; (ii) $n_f = 1$, $n_s = 0.3$, $n_n = 0$; (iii) $n_f = 1$, $n_s = 0$, $n_n = 0$; (iv) $n_f = 0.7$, $n_s = 0$, $n_n = 0.3$; (v) $n_f = 1$, $n_s = 0$, $n_n = 0.3$. Apart from the prescribed proportion of active tension, the settings are the same as the baseline simulation[2] presented in Section 4.2.

[2] Notice that case iv is the baseline simulation.

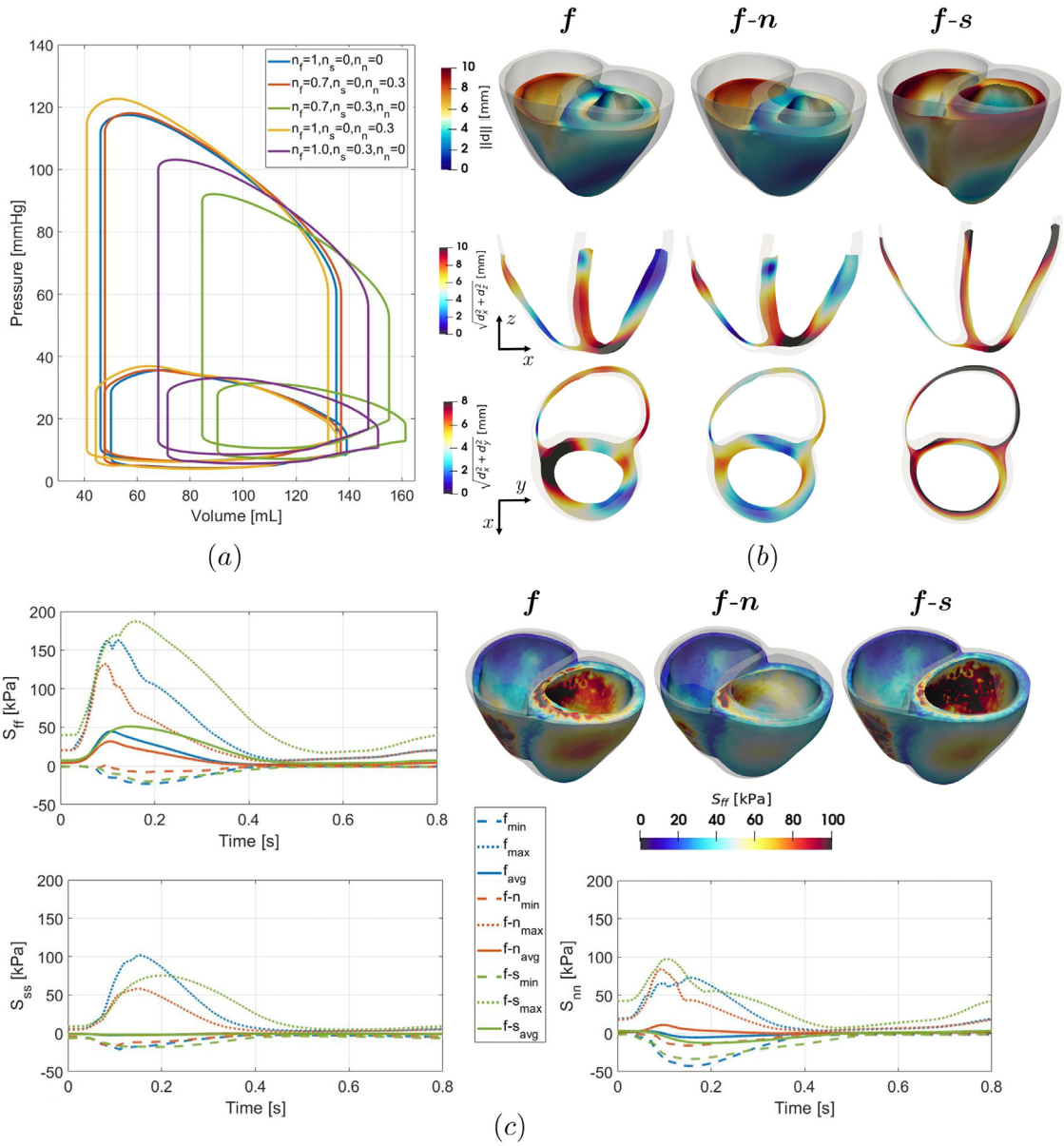

Fig. 6. Cross-fibers active contraction EM simulations; (a) PV-loops from several cross-fibers active contraction arrangements built by setting in Eq. (3) different combinations of n_{f}, n_{s} and n_{n}; (b) mechanical displacements (top) and mid ventricular slices at the end of systole ($t = 0.35\,\mathrm{s}$), showing LFS (middle) and WT (bottom), colored by the in-plane displacement magnitude (i.e $\sqrt{d_x^2 + d_z^2}$ for LFS and $\sqrt{d_x^2 + d_y^2}$ for WT), for redistributed cross-fibers active contraction configurations: a pure fiber $\boldsymbol{f}$, a fiber-normal $\boldsymbol{f-n}$ and a fiber-sheet $\boldsymbol{f-s}$ contraction; (c) circumferential stress S_{ff} (top-right) at the peak pressure time instant ($t = 0.1\,\mathrm{s}$) and the time trace of the average, minimum and maximum axial stresses S_{ff} (top-left), S_{ss} (bottom-left) and S_{nn} (bottom-right) for $\boldsymbol{f}$, $\boldsymbol{f-n}$ and $\boldsymbol{f-s}$ configurations.

Fig. 6(a) shows the PV-loops from the five cases. An active tension along the sheet direction ($n_{\mathrm{s}} > 0$, cases i and ii) produces a PV-loop with a reduced area compared to case iii with no cross-fibers active contraction. Conversely, an active tension along the normal direction ($n_{\mathrm{n}} > 0$, cases iv and v) yields a PV-loop with an increased area. Table 5 displays, for all the cases, the ejection fraction ($\mathrm{EF_i}$) and the stroke volume ($\mathrm{SV_i} = \mathrm{EDV_i} - \mathrm{ESV_i}$) of the left (i = LV) and right (i = RV) ventricles. The maximal cardiac work is achieved for case v while the minimal for case i. The above analysis shows that the active tension along the sheet direction ($n_{\mathrm{s}} > 0$) counteracts the

Table 5
Ejection fraction (EF_i) of the left (i = LV) and right (i = RV) ventricles for the different cross-fibers active contraction cases i–v. The stroke volume (SV_i) of the two ventricles is also shown.

Cross-fiber configuration	EF_{LV}	EF_{RV}	SV_{LV}	SV_{RV}
(i) $n_f = 0.7$, $n_s = 0.3$, $n_n = 0$	45 %	44 %	70.69 mL	71.04 mL
(ii) $n_f = 1$, $n_s = 0.3$, $n_n = 0$	54 %	53 %	79.40 mL	79.50 mL
(iii) $n_f = 1$, $n_s = 0$, $n_n = 0$	65 %	64 %	89.14 mL	89.08 mL
(iv) $n_f = 0.7$, $n_s = 0$, $n_n = 0.3$	66 %	65 %	89.27 mL	89.23 mL
(v) $n_f = 1$, $n_s = 0$, $n_n = 0.3$	69 %	67 %	91.14 mL	91.09 mL

Table 6
LFS and WT for the three configurations of redistributed myofibers active contraction ($\boldsymbol{f}$, $\boldsymbol{f}-\boldsymbol{n}$ and $\boldsymbol{f}-\boldsymbol{s}$).

Cross-fiber configuration	LFS	WT
(iii) $\boldsymbol{f}$	17 %	30 %
(iv) $\boldsymbol{f}-\boldsymbol{n}$	21 %	41 %
(i) $\boldsymbol{f}-\boldsymbol{s}$	7 %	8 %

myofiber contraction, while the one along the normal direction ($n_n > 0$) enhances the cardiac work, in accordance to [31,58].

In order to better appreciate the differences among the cross-fibers active contraction arrangements, we further compared cases i and iv with case iii. In these particular cases, the proportion of active tension sums up to 1 ($n_f + n_s + n_n = 1$), meaning that the myofibers contraction is redistributed along the three directions: case iii ($n_f = 1$, $n_s = 0$, $n_n = 0$) is a pure fiber contraction, in the following denoted by $\boldsymbol{f}$ configuration; case i ($n_f = 0.7$, $n_s = 0$, $n_n = 0.3$) is a contraction in the fiber and normal directions, hereafter indicated by $\boldsymbol{f}-\boldsymbol{n}$ configuration; case iv ($n_f = 0.7$, $n_s = 0.3$, $n_n = 0$) is a contraction along the fiber and sheet directions, named $\boldsymbol{f}-\boldsymbol{s}$ configuration.

Fig. 6(b) illustrates the mechanical displacements at the end of systole ($t = 0.35$ s) for the three considered configurations ($\boldsymbol{f}$, $\boldsymbol{f}-\boldsymbol{n}$ and $\boldsymbol{f}-\boldsymbol{s}$). Both the apico-basal shortening and the wall thickening is dramatically reduced for $\boldsymbol{f}-\boldsymbol{s}$ configuration. Almost the same mechanical contraction is achieved for $\boldsymbol{f}$ and $\boldsymbol{f}-\boldsymbol{n}$ configurations with a slightly more pronounced longitudinal shortening and wall thickening for $\boldsymbol{f}-\boldsymbol{n}$ configuration. The LFS and WT are reported in Table 6.

We also evaluate the components of the mechanical stress by means of the following indicators [46]:

$$S_{ff} = (\mathbf{P}\mathbf{f}_0)\cdot\frac{\mathbf{F}\mathbf{f}_0}{|\mathbf{F}\mathbf{f}_0|}, \quad S_{ss} = (\mathbf{P}\mathbf{s}_0)\cdot\frac{\mathbf{F}\mathbf{s}_0}{|\mathbf{F}\mathbf{s}_0|}, \quad S_{nn} = (\mathbf{P}\mathbf{n}_0)\cdot\frac{\mathbf{F}\mathbf{n}_0}{|\mathbf{F}\mathbf{n}_0|},$$

where $\mathbf{f}_0$, $\mathbf{s}_0$ and $\mathbf{n}_0$ are the myofiber directions, $\mathbf{P}$ is the first Piola–Kirchhoff stress tensor and $\mathbf{F}$ is the deformation gradient tensor. The metric S_{aa} (with a = f, s, n) measures the axial stresses along the circumferential (a = f), radial (a = s) and longitudinal (a = n) directions.

Fig. 6(c) displays, for the three configurations $\boldsymbol{f}$, $\boldsymbol{f}-\boldsymbol{n}$ and $\boldsymbol{f}-\boldsymbol{s}$, the circumferential stress (S_{ff}) at the peak pressure time instant ($t = 0.1$ s) and the time trace of the average, minimum and maximum axial stresses S_{ff}, S_{ss} and S_{nn}. The circumferential stress at the peak pressure instant is much higher, especially on LV side, for $\boldsymbol{f}-\boldsymbol{s}$ configuration with respect to the other two. Conversely, $\boldsymbol{f}-\boldsymbol{n}$ configuration produces the lowest circumferential stress. Almost the same considerations hold for the time trace of the three axial stresses during the complete cardiac cycle, see Fig. 6(c).

4.4. Impact of myofiber architecture on the electromechanical function

We investigate the effect of different myofibers architecture on the biventricular EM model, by considering three types of LDRBMs: D-RBM, B-RBM and R-RBM (see Section 2.1). Apart from the employed LDRBM, used to prescribe the myofibers architecture, all the other settings, including the fiber input angles (8), are the same as the baseline simulation[3] presented in Section 4.2.

[3] Notice that the case with D-RBM is the baseline simulation.

Table 7
Comparison of relevant mechanical biomarkers among the electromechanical simulations by employing different LDRBMs (D-RBM,B-RBM and R-RBM) to prescribe the myofiber architecture.

Mechanical biomarkers	D-RBM	B-RBM	R-RBM
EDV_{LV} (mL)	137	145	138
EDV_{RV} (mL)	138	136	139
ESV_{LV} (mL)	48	58	50
ESV_{RV} (mL)	49	49	50
EF_{LV} (%)	66	60	64
EF_{RV} (%)	65	64	64
P_{LV} (mmHg)	117	114	117
P_{RV} (mmHg)	35	34	33
LFS (%)	21	25	20
WT (%)	41	36	38

Fiber orientations obtained for the three LDRBMs (D-RBM, B-RBM and R-RBM) in the Zygote biventricular model are shown in Fig. 7(a). For a detailed comparison among the three LDRBMs we refer the reader to [47], where pure electrophysiological simulations were considered. Here, we are instead interested in the effect on mechanical quantities obtained by means of EM model. We recall that B-RBM produces a smooth change in the fiber field in the transition across the two ventricles, while R-RBM and D-RBM a strong discontinuity [47]. Moreover, R-RBM and D-RBM feature a linear transition passing from the endocardium to the epicardium, while B-RBM employs a bidirectional spherical interpolation *bislerp* (see [47,52,54,55]).

In Fig. 7(b) the PV-loop curves (for both ventricles) are displayed, while in Table 7 some relevant mechanical biomarkers are compared among the simulation results. The left ventricular PV-loop area of B-RBM is shifted towards larger volumes with respect to the ones of D-RBM and R-RBM that show almost a compatible PV-loop for LV, see Fig. 7(b, top). Moreover, the left systolic pressure peak decreases for B-RBM with respect to D-RBM and R-RBM, see Figs. 7(b, top) and Table 7. As a consequence, the left ventricular ejection fraction obtained with B-RBM (60%) is smaller than those obtained with D-RBM and R-RBM (66% and 65%, respectively), see Table 7. On the contrary, small differences are observed for the right ventricular PV-loops with only a slightly larger ejection fraction for D-RBM, see Fig. 7(b, bottom) and Table 7.

Fig. 7(d) shows the circumferential stress (S_{ff}) at the peak pressure instant ($t = 0.1$ s) and the time trace of the average, minimum and maximum axial stresses S_{ff}, S_{ss} and S_{nn}. The patterns of S_{ff} are very similar for the three methods, see Fig. 7(d, top-right). Instead, the time traces of the axial stresses present several discrepancies. Specifically, S_{ff} reveals lower values obtained by B-RBM with respect to D-RBM and R-RBM, see Fig. 7(d, top-left). This is associated to a lower cardiac work produced by B-RBM ($EF_{LV} = 60\%$) compared to D-RBM and R-RBM ($EF_{LV} = 66\%$, 64%, respectively). On the contrary, the longitudinal stress S_{nn} presents an opposite trend, see Fig. 7(d, bottom-right). This is ascribed to a larger apico-basal shortening for B-RBM (LFS $= 25\%$) with respect to D-RBM and R-RBM (LFS $= 21\%$, 20%, respectively). Meanwhile, larger values of the radial stress S_{ss} are observed for D-RBM with respect to B-RBM and R-RBM, see Fig. 7(d,bottom-right), associated to a larger wall thickening of D-RBM (WT $= 41\%$) against the ones of R-RBM and B-RBM (WT $= 38\%$, 36%, respectively).

5. Discussion

We presented a 3D biventricular EM model coupled with a 0D closed-loop model of the whole circulatory system. This mathematical and numerical model represents an extension of the one proposed in [15,46] for the LV. Differently from previous works in the literature focusing on Windkessel-type preload/afterload models [33–38], here we considered a closed-loop 0D model of the whole cardiovascular system. With respect to other biventricular EM models [28,32], we derived proper boundary conditions with uniform and weighted stress distributions, that account for the neglected part of the domain above the biventricular base and satisfy the principles of momentum and energy conservation. Furthermore, our numerical strategy does not require adaptations through the different phases of the heartbeat. Consequently, the 3D–0D biventricular model can be effectively used to address rhythm disorders, such as ventricular tachycardia [114].

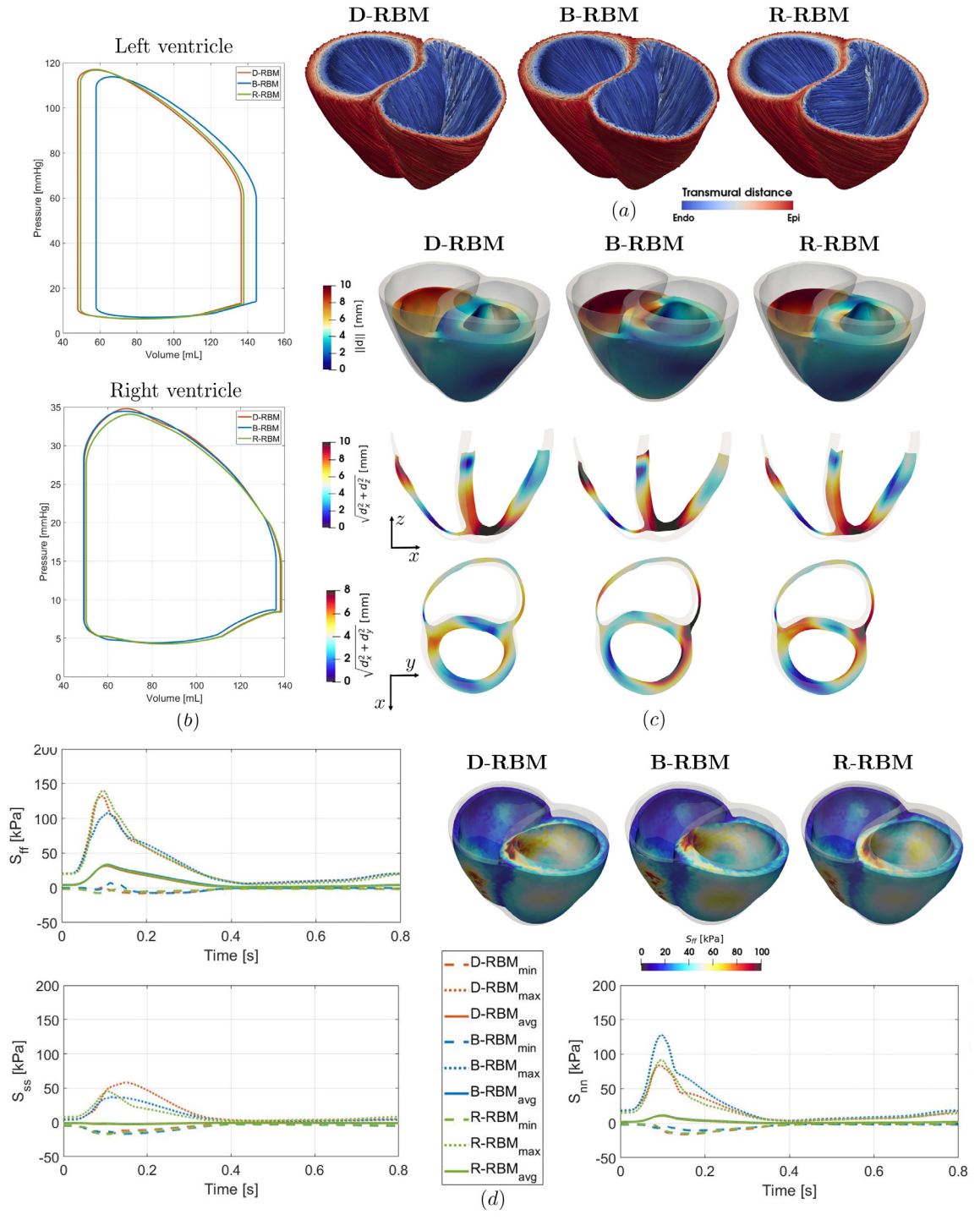

Fig. 7. Results of the EM simulations employing different LDRBMs (R-RBM, B-RBM and D-RBM); (a) fiber orientations obtained for the three LDRBMs; (b) PV-loop curves, for LV (top) and RV (bottom), obtained with D-RBM (orange), B-RBM (blue) and R-RBM (green); (c) mechanical displacements (top) and mid ventricular slices at the end of systole ($t = 0.35$ s), showing LFS (middle) and WT (bottom), colored by the in-plane displacement magnitude (i.e $\sqrt{d_x^2 + d_z^2}$ for LFS and $\sqrt{d_x^2 + d_y^2}$ for WT); (d) circumferential stress S_{ff} (top-right) at the peak pressure instant ($t = 0.1$ s) and the time trace of the average, minimum and maximum axial stresses S_{ff} (top-left), S_{ss} (bottom-left) and S_{nn} (bottom-right) for the three LDRBMs. (For interpretation of the references to color in this figure legend, the reader is referred to the web version of this article.)

The numerical results obtained on a realistic biventricular geometry, after a suitable parameter calibration, quantitatively match the experimental data of relevant mechanical biomarkers available in the literature, such as the end systolic and diastolic volumes, the ejection fraction and the systolic pressure peak [66–72]. In particular, thanks to the novel weighted stress distributions basal boundary condition, we were able to obtain physiological longitudinal fractional shortening. Conversely, the majority of ventricular EM models have limitations in reproducing the longitudinal systolic shortening, as excluding the atria from the geometry requires to fix the basal plane or restrict its radial motion [24,27,32,78,115]. This is in contrast with physiological contraction where the atrioventricular plane displacement moves significantly downwards in the apico-basal direction [98,116].

We also investigated the impact of fiber dispersion by partially redistributing active tension on cross-fiber directions. We noticed that an active tension along the sheetlet direction yields to an unphysiological cardiac work, with ejection fraction, longitudinal shortening and wall thickening below the physiological ranges (see Tables 4–6). On the contrary, active tension on the sheet-normal direction contributes to a more effective cardiac contraction with a much lower axial stress with respect to a non-dispersed fiber configuration. These results are in accordance with [31,58].

Finally, we performed for the first time a sensitivity analysis by looking at EM outputs in the limit cycle when considering D-RBM, B-RBM and R-RBM to generate the cardiac fibers [47]. We showed that there is a strong interaction between LV and RV [20]. A different fiber architecture in the transmural wall (from epicardium to endocardium) and a dissimilar septal fiber interconnection between the two ventricles affect the ventricular cardiac pump work, in particular the LV one. This highlights the importance of considering the two chambers together during ventricular EM simulations. Indeed, the continuous interrelationships between right and left ventricular functions are well known not only in physiological conditions, but particularly in pathological situations, for which any pressure and/or volume overload of a ventricle is instantaneously reflected in impairment of the function of the contralateral ventricle.

A limitation of the proposed model is that the force generation model (RDQ18, [92]) does not take into account the feedback of the fibers contraction velocity (force–velocity relationship). This causes the sharp pressure peak displayed in Fig. 5(d), which would be smoothed by using a model that takes into account the force–velocity relationship, such as the RDQ20 model, as shown in [81]. Another limitation consisted in the use of a surrogate model of the Purkinje system (by means of the fast endocardial conduction layer [73]) instead of an explicitly modelization of such network (as done in [88–90]). Although this approximation is reasonable in physiological condition, the Purkinje network should be explicitly modeled in order to achieve a more realistic activation sequence in the ventricles, in particular when attempting to reproduce pathological conditions, like for instance the Left Bundle Branch Block [88]. A further improvement will be given by validating the results against measures coming from medical imaging, such as myocardial displacement by cine-MRI or ejection fraction/stroke volume from echo-cardiography.

6. Conclusions

In this work, we proposed a 3D–0D closed-loop model of biventricular cardiac EM. We provided a rigorous mathematical and numerical formulation of the 3D–0D model by fully detailing our approach to couple the 3D and the 0D models. We carried out several numerical simulations aimed at reproducing physiological quantities like the end systolic and diastolic volumes, the ejection fractions, the systolic pressure peaks, the longitudinal fractional shortening and the fractional wall thickening. We studied different configurations in cross-fibers active contraction highlighting that the proportion of active tension along the sheet direction should be avoided in the framework of an orthotropic active stress. Finally, we evaluated the impact of different myofibers architecture on the biventricular EM, showing the importance of considering a biventricular model with respect to a stand-alone LV model.

Declaration of competing interest

The authors declare that they have no known competing financial interests or personal relationships that could have appeared to influence the work reported in this paper.

Acknowledgments

This project has received funding from the European Research Council (ERC) under the European Union's Horizon 2020 research and innovation program (grant agreement No 740132, iHEART — An Integrated Heart Model for the simulation of the cardiac function, P.I. Prof. A. Quarteroni). We acknowledge the CINECA award under the class C ISCRA project HP10C3Z520 for the availability of high performance computing resources.

Appendix A. Model parameters

We provide the list of parameters adopted for the simulations in Section 4. In particular, Table 8 contains the parameters of the 3D EM model (referred to $\mathscr{E}$, $\mathscr{A}$, $\mathscr{M}$) and Table 9 those of the 0D closed-loop hemodynamic model ($\mathscr{C}$). Moreover, for the TTP06 ionic model, we use the parameters (for epicardium cells) reported in [91], while for the RDQ18 model, we employ those in [82].

Appendix B. Energy-consistent boundary condition in biventricular geometries

The energy-consistent boundary condition (2.9) accounts for the effect of the neglected part of the domain located above the biventricular base Γ_0^{base} (which is an artificial boundary), consistently with the principles of momentum and energy conservation. It represents a generalization of the boundary condition proposed in [82] for biventricular geometries. In what follows, we denote by $\Omega_t^{\text{fluid,LV}}$ (respectively $\Omega_t^{\text{fluid,RV}}$) the volume occupied at time t, within LV (respectively, RV), by the fluid located below the base. Moreover, we employ the tilde symbol ($\sim$) to refer to volumes and surfaces located above the ventricular base. Specifically, we denote by $\widetilde{\Omega}_t^{\text{fluid,LV}}$ and $\widetilde{\Omega}_t^{\text{fluid,RV}}$ the fluid volumes in LV and RV, located above the base. Similarly, we denote by $\widetilde{\Gamma}_t^{\text{epi}}$, $\widetilde{\Gamma}_t^{\text{endo,LV}}$ and $\widetilde{\Gamma}_t^{\text{endo,RV}}$ the epicardial, and endocardial (left and right) surfaces located above the ventricular base. Finally, we denote by $\widetilde{\Gamma}_t^{\text{base}}$ the ventricular base surface itself, but endowed with outer normal vector directed towards the apex, differently than for Γ_t^{base}.

Following the derivation of [82] and by defining the Cauchy stress tensor as $\mathbf{T} = J^{-1}\mathbf{P}\mathbf{F}^T$, with a quasi-static approximation the balance of momentum entails

$$\mathbf{0} = \int_{\widetilde{\Omega}_t} \nabla \cdot \mathbf{T}\, d\mathbf{x} = \int_{\partial\widetilde{\Omega}_t} \mathbf{T}\mathbf{n}\, d\Gamma_t = \int_{\widetilde{\Gamma}_t^{\text{epi}}} \mathbf{T}\mathbf{n}\, d\Gamma_t + \int_{\widetilde{\Gamma}_t^{\text{endo,LV}}} \mathbf{T}\mathbf{n}\, d\Gamma_t + \int_{\widetilde{\Gamma}_t^{\text{endo,RV}}} \mathbf{T}\mathbf{n}\, d\Gamma_t + \int_{\widetilde{\Gamma}_t^{\text{base}}} \mathbf{T}\mathbf{n}\, d\Gamma_t. \tag{9}$$

The normal stress on the endocardium is given by $\mathbf{T}\mathbf{n} = -p_{\text{LV}}\mathbf{n}$ (on $\widetilde{\Gamma}_t^{\text{endo,LV}}$) and $\mathbf{T}\mathbf{n} = -p_{\text{RV}}\mathbf{n}$ (on $\widetilde{\Gamma}_t^{\text{endo,RV}}$), while we assume negligible the load on the epicardium (i.e. $\mathbf{T}\mathbf{n} = \mathbf{0}$ on $\widetilde{\Gamma}_t^{\text{epi}}$). Thanks to the divergence (Gauss) theorem, it is possible to write the endocardial terms of the summation of Eq. (9) as integrals over $\Gamma_t^{\text{endo,LV}}$ and $\Gamma_t^{\text{endo,RV}}$. Indeed, we have the identity:

$$\mathbf{0} = \int_{\Omega_t^{\text{fluid,LV}} \cup \widetilde{\Omega}_t^{\text{fluid,LV}}} \nabla p_{\text{LV}}\, d\mathbf{x} = \int_{\Gamma_t^{\text{endo,LV}}} p_{\text{LV}}\mathbf{n}\, d\Gamma_t + \int_{\widetilde{\Gamma}_t^{\text{endo,LV}}} p_{\text{LV}}\mathbf{n}\, d\Gamma_t,$$

and similarly for the RV we have $\int_{\widetilde{\Gamma}_t^{\text{endo,RV}}} p_{\text{LV}}\mathbf{n}\, d\Gamma_t = -\int_{\Gamma_t^{\text{endo,RV}}} p_{\text{RV}}\mathbf{n}\, d\Gamma_t$. Hence, we end up with the following identity

$$\begin{aligned}\int_{\Gamma_t^{\text{base}}} \mathbf{T}\mathbf{n}\, d\Gamma_t &= -\int_{\widetilde{\Gamma}_t^{\text{base}}} \mathbf{T}\mathbf{n}\, d\Gamma_t = -\int_{\widetilde{\Gamma}_t^{\text{endo,LV}}} p_{\text{LV}}\mathbf{n}\, d\Gamma_t - \int_{\widetilde{\Gamma}_t^{\text{endo,RV}}} p_{\text{RV}}\mathbf{n}\, d\Gamma_t \\ &= \int_{\Gamma_t^{\text{endo,LV}}} p_{\text{LV}}\mathbf{n}\, d\Gamma_t + \int_{\Gamma_t^{\text{endo,RV}}} p_{\text{RV}}\mathbf{n}\, d\Gamma_t,\end{aligned}$$

which entails, by considering the pull-back, to the reference configuration

$$\int_{\Gamma_t^{\text{base}}} \mathbf{T}\mathbf{n}\, d\Gamma_t = \int_{\Gamma_0^{\text{endo,LV}}} p_{\text{LV}}\, J\mathbf{F}^{-T}\mathbf{n}\, d\Gamma_0 + \int_{\Gamma_0^{\text{endo,RV}}} p_{\text{RV}}\, J\mathbf{F}^{-T}\mathbf{n}\, d\Gamma_0. \tag{10}$$

Table 8
Input parameters of the 3D EM model.

Variable	Value	Unit	Description
Electrophysiology			
T_{hb}	0.8	s	Heartbeat duration
χ_{m}	1	$\mu\text{F/cm}^2$	Surface-to-volume ratio
C_{m}	1400	cm^{-1}	Transmembrane capacitance
ϵ	0.01	–	Threshold of the fast conduction layer
$(\sigma_{\ell,\text{fast}}, \sigma_{\text{t,fast}}, \sigma_{\text{n,fast}})$	(4.28, 1.96, 0.64)	mS/cm	Fast layer conductivities
$(\sigma_{\ell,\text{myo}}, \sigma_{\text{t,myo}}, \sigma_{\text{n,myo}})$	(1.07, 0.49, 0.16)	mS/cm	Myocardial conductivities
$\mathcal{I}_{\text{app}}$	$50 \cdot 10^3$	$\mu\text{A/cm}^3$	Applied current value
t_{app}	3.0	ms	Applied current duration
$t^0_{\text{LV,app}}$	(0.0,0.0,0.0)	ms	Applied current LV initial times
$t^0_{\text{RV,app}}$	(5.0,5.0)	ms	Applied current RV initial times
δ_{app}	$2.5 \cdot 10^{-3}$	m	Applied current radius
Mechanics			
ρ_{s}	10^3	kg m^{-3}	Tissue density
$K^{\text{epi}}_{\parallel}$	$2 \cdot 10^4$	Pa m^{-1}	Normal stiffness of epicardium
$K^{\text{epi}}_{\perp}$	$2 \cdot 10^5$	Pa m^{-1}	Tangential stiffness of epicardial tissue
$C^{\text{epi}}_{\perp}$	$2 \cdot 10^4$	Pa s m^{-1}	Normal viscosity of epicardial tissue
$C^{\text{epi}}_{\parallel}$	$2 \cdot 10^3$	Pa s m^{-1}	Tangential viscosity of epicardial tissue
a	$0.88 \cdot 10^3$	Pa	Material stiffness
k	$50 \cdot 10^3$	Pa	Bulk modulus
b_{ff}	8	–	Fiber strain scaling
b_{ss}	6	–	Radial strain scaling
b_{nn}	3	–	Cross-fiber in-plain strain scaling
b_{fs}	12	–	Shear strain in fiber-sheet plane scaling
b_{fn}	3	–	Shear strain in fiber-normal plane scaling
b_{sn}	3	–	Shear strain in sheet-normal plane scaling
Reference configuration			
$\widetilde{p}_{\text{LV}}$	600	Pa	Residual left ventricular pressure
$\widetilde{p}_{\text{RV}}$	400	Pa	Residual right ventricular pressure
$\widetilde{T}_{\text{a}}$	$350 \cdot 10^3$	Pa	Residual active tension
C_{lrv}	1	–	Residual contractility ratio
Activation			
SL_0	2	μm	Reference sarcomere length
$T^{\text{max}}_{\text{a}}$	$840 \cdot 10^3$	Pa	Maximum tension
C_{lrv}	0.60	–	Contractility ratio

Eq. (10) provides the overall stress acting on the ventricular base. However, we need some additional assumptions to define the point-wise distribution of stress, among the infinitely many satisfying Eq. (10). In the original derivation of the energy-consistent boundary condition [82], at this stage, a uniform stress distribution assumption is made. However, while this assumption is reasonable in a single-ventricle geometry, it is unrealistic when the ventricular base surrounds both ventricles. Indeed, the pressures acting in LV are typically much larger than those in RV. For this reason, we propose to distribute stress over the gamma surface not uniformly, but rather according to a weight function $\phi : \Gamma_0^{\text{base}} \to [0, 1]$, that indicates the fraction of stress attributable to the pressure acting on LV, relative RV, at each base point. Hence, we assume that, on Γ_0^{base}, we have:

$$\mathbf{Tn} = \phi \frac{\int_{\Gamma_0^{\text{endo,LV}}} p_{\text{LV}}\, J\mathbf{F}^{-T}\mathbf{n}\, d\Gamma_0}{\int_{\Gamma_t^{\text{base}}} \phi\, d\Gamma} + (1-\phi)\frac{\int_{\Gamma_0^{\text{endo,RV}}} p_{\text{RV}}\, J\mathbf{F}^{-T}\mathbf{n}\, d\Gamma_0}{\int_{\Gamma_t^{\text{base}}} (1-\phi)\, d\Gamma}, \tag{11}$$

which reads, in the reference configuration:

$$\mathbf{Pn} = |J\mathbf{F}^{-T}\mathbf{n}| \left[\phi \frac{\int_{\Gamma_0^{\text{endo,LV}}} p_{\text{LV}}\, J\mathbf{F}^{-T}\mathbf{n}\, d\Gamma_0}{\int_{\Gamma_0^{\text{base}}} |J\mathbf{F}^{-T}\mathbf{n}|\, \phi\, d\Gamma_0} + (1-\phi)\frac{\int_{\Gamma_0^{\text{endo,RV}}} p_{\text{RV}}\, J\mathbf{F}^{-T}\mathbf{n}\, d\Gamma_0}{\int_{\Gamma_0^{\text{base}}} |J\mathbf{F}^{-T}\mathbf{n}|\, (1-\phi)\, d\Gamma_0} \right]. \tag{12}$$

Table 9
Input parameters of the 0D closed-loop hemodynamic model.

Variable	Value	Unit	Description
Circulation			
R_{AR}^{SYS}	0.416	mmHg s mL^{-1}	Resistance of systemic arterial system
R_{VEN}^{SYS}	0.260	mmHg s mL^{-1}	Resistance of systemic venous system
R_{AR}^{PUL}	0.048	mmHg s mL^{-1}	Resistance of pulmonary arterial system
R_{VEN}^{PUL}	0.036	mmHg s mL^{-1}	Resistance of pulmonary venous system
C_{AR}^{SYS}	1.62	mL mmHg^{-1}	Capacitance of systemic arterial system
C_{VEN}^{SYS}	60.00	mL mmHg^{-1}	Capacitance of systemic venous system
C_{AR}^{PUL}	5.00	mL mmHg^{-1}	Capacitance pulmonary arterial system
C_{VEN}^{PUL}	16.00	mL mmHg^{-1}	Capacitance of pulmonary venous system
L_{AR}^{SYS}	$5 \cdot 10^{-3}$	mmHg s^2 mL^{-1}	Impedance of systemic arterial system
L_{VEN}^{SYS}	$5 \cdot 10^{-4}$	mmHg s^2 mL^{-1}	Impedance of systemic venous system
L_{AR}^{PUL}	$5 \cdot 10^{-4}$	mmHg s^2 mL^{-1}	Impedance pulmonary arterial system
L_{VEN}^{PUL}	$5 \cdot 10^{-4}$	mmHg s^2 mL^{-1}	Impedance of pulmonary venous system
E_{LA}^{A}	0.09	mmHg mL^{-1}	Left atrium elastance amplitude
E_{RA}^{A}	0.06	mmHg mL^{-1}	Right atrium elastance amplitude
E_{LA}^{B}	0.07	mmHg mL^{-1}	Left atrium elastance baseline
E_{RA}^{B}	0.07	mmHg mL^{-1}	Right atrium elastance baseline
T_{LA}^{ac}	0.17	–	Duration of left atrium contraction (w.r.t. T_{hb})
T_{RA}^{ac}	0.17	–	Duration of right atrium contraction (w.r.t. T_{hb})
t_{LA}^{ac}	0.80	–	Initial time of left atrium contraction (w.r.t. T_{hb})
t_{RA}^{ac}	0.80	–	Initial time of right atrium contraction (w.r.t. T_{hb})
T_{LA}^{ar}	0.17	–	Duration of left atrium relaxation (w.r.t. T_{hb})
T_{RA}^{ar}	0.17	–	Duration of right atrium relaxation (w.r.t. T_{hb})
$V_{0,LA}$	4.0	mL	Left atrium resting volume
$V_{0,RA}$	4.0	mL	Right atrium resting volume
R_{min}	$75 \cdot 10^{-4}$	mmHg s mL^{-1}	Valves minimal resistance
R_{max}	$75 \cdot 10^{3}$	mmHg s mL^{-1}	Valves maximum resistance

In what follows we consider three different choices for the weight function ϕ, corresponding to as many boundary condition formulations.

- **Uniform stress distribution**. By setting $\phi \equiv \frac{1}{2}$, we recover the case of stress uniformly distributed on the whole Γ_0^{base} boundary:

$$\mathbf{Pn} = \frac{|J\mathbf{F}^{-T}\mathbf{n}|}{\int_{\Gamma_0^{base}} |J\mathbf{F}^{-T}\mathbf{n}| d\Gamma_0} \left[\int_{\Gamma_0^{endo,LV}} p_{LV}\, J\mathbf{F}^{-T}\mathbf{n}\, d\Gamma_0 + \int_{\Gamma_0^{endo,RV}} p_{RV}\, J\mathbf{F}^{-T}\mathbf{n}\, d\Gamma_0 \right] \tag{13}$$

- **Uniform stress distribution over each base**. Let us suppose to split the base into two subsets $\Gamma_0^{base,LV}$ and $\Gamma_0^{base,RV}$, respectively denoting the portion of ventricular base surrounding LV and RV. Then, we define ϕ as the indicator function of the set $\Gamma_0^{base,LV}$ (that is $\phi = 1$ on $\Gamma_0^{base,LV}$, while $\phi = 0$ on $\Gamma_0^{base,RV}$). In this case, we

get:

$$\begin{cases} \mathbf{Pn} = \dfrac{|J\mathbf{F}^{-T}\mathbf{n}|}{\int_{\Gamma_0^{\text{base,LV}}} |J\mathbf{F}^{-T}\mathbf{n}| d\Gamma_0} \displaystyle\int_{\Gamma_0^{\text{endo,LV}}} p_{\text{LV}}\, J\mathbf{F}^{-T}\mathbf{n}\, d\Gamma_0 & \text{on } \Gamma_0^{\text{base,LV}} \\ \mathbf{Pn} = \dfrac{|J\mathbf{F}^{-T}\mathbf{n}|}{\int_{\Gamma_0^{\text{base,RV}}} |J\mathbf{F}^{-T}\mathbf{n}| d\Gamma_0} \displaystyle\int_{\Gamma_0^{\text{endo,RV}}} p_{\text{RV}}\, J\mathbf{F}^{-T}\mathbf{n}\, d\Gamma_0 & \text{on } \Gamma_0^{\text{base,RV}} \end{cases} \tag{14}$$

- **Weighted stress distribution**. Finally, we consider the case in which we set $\phi = \hat{\xi}$ (as defined in Section 2.1). The function $\hat{\xi}$ is defined such that we have $\hat{\xi} \simeq 1$ on $\Gamma_0^{\text{base,LV}}$, $\hat{\xi} \simeq 0$ on $\Gamma_0^{\text{base,RV}}$ and we have a smooth transition on the septum. With this choice, the energy-consistent boundary condition of Eq. (12) reads

$$\mathbf{Pn} = |J\mathbf{F}^{-T}\mathbf{N}| \left[p_{\text{LV}}(t)\mathbf{v}_{\text{LV}}^{\text{base}}(\boldsymbol{x}, t) + p_{\text{RV}}(t)\mathbf{v}_{\text{RV}}^{\text{base}}(\boldsymbol{x}, t) \right], \tag{15}$$

having defined the vectors $\mathbf{v}_{\text{LV}}^{\text{base}}$ and $\mathbf{v}_{\text{RV}}^{\text{base}}$ as in Eq. (4).

Based upon our experience, the uniform stress distribution approach does not typically provide meaningful results. Indeed, since the stress is redistributed on the whole base without accounting for the closeness to the two chambers, a net angular momentum results on the elastic body, making it rotate during systole. Conversely, both the uniform stress distribution approach over each base and the weighted stress distribution approach overcome this issue, thanks to a more realistic distribution of the stress. While the two strategies globally provide very similar results, the latter allows for a smoother solution close to the interface between the left and right bases. For this reason, in this paper we focus on the weighted stress distribution approach.

Appendix C. 3D-0D saddle-point problem resolution

We solve the non-linear saddle-point problem (7) by means of the following Newton algorithm (where the subscript $n+1$ is understood):

- We set $\mathbf{d}_{\text{h}}^{(0)} = \mathbf{d}_{\text{h}}^{n}$, $p_{\text{LV}}^{(0)} = p_{\text{LV}}^{n}$ and $p_{\text{RV}}^{(0)} = p_{\text{RV}}^{n}$
- For $j = 1, 2, \ldots,$ until convergence, we solve the linear system

$$\begin{pmatrix} J_{\mathbf{d},\mathbf{d}}^{(j-1)} & J_{\mathbf{d},p_{\text{LV}}}^{(j-1)} & J_{\mathbf{d},p_{\text{RV}}}^{(j-1)} \\ J_{p_{\text{LV}},\mathbf{d}}^{(j-1)} & 0 & 0 \\ J_{p_{\text{RV}},\mathbf{d}}^{(j-1)} & 0 & 0 \end{pmatrix} \begin{pmatrix} \Delta\mathbf{d}_{\text{h}}^{(j)} \\ \Delta p_{\text{LV}}^{(j)} \\ \Delta p_{\text{RV}}^{(j)} \end{pmatrix} = \begin{pmatrix} \mathbf{r}_{\mathbf{d}}^{(j-1)} \\ r_{p_{\text{LV}}}^{(j-1)} \\ r_{p_{\text{RV}}}^{(j-1)} \end{pmatrix}, \tag{16}$$

  where
  $J_{\mathbf{d},\mathbf{d}}^{(j-1)} = \frac{\partial}{\partial \mathbf{d}} \mathbf{r}_{\mathbf{d}}(\mathbf{d}_{\text{h}}^{(j-1)}, p_{\text{LV}}^{(j-1)}, p_{\text{RV}}^{(j-1)})$,
  $J_{\mathbf{d},p_{\text{LV}}}^{(j-1)} = \frac{\partial}{\partial p_{\text{LV}}} \mathbf{r}_{\mathbf{d}}(\mathbf{d}_{\text{h}}^{(j-1)}, p_{\text{LV}}^{(j-1)}, p_{\text{RV}}^{(j-1)})$, $J_{\mathbf{d},p_{\text{RV}}}^{(j-1)} = \frac{\partial}{\partial p_{\text{RV}}} \mathbf{r}_{\mathbf{d}}(\mathbf{d}_{\text{h}}^{(j-1)}, p_{\text{LV}}^{(j-1)}, p_{\text{RV}}^{(j-1)})$,
  $J_{p_{\text{LV}},\mathbf{d}}^{(j-1)} = \frac{\partial}{\partial \mathbf{d}} r_{p_{\text{LV}}}(\mathbf{d}_{\text{h}}^{(j-1)})$, $J_{p_{\text{RV}},\mathbf{d}}^{(j-1)} = \frac{\partial}{\partial \mathbf{d}} r_{p_{\text{RV}}}(\mathbf{d}_{\text{h}}^{(j-1)})$.
  In our implementation, the Jacobian matrix is computed by means of automatic differentiation.
- We update
  $\mathbf{d}_{\text{h}}^{(j)} = \mathbf{d}_{\text{h}}^{(j-1)} - \Delta\mathbf{d}_{\text{h}}^{(j)}$, $p_{\text{LV}}^{(j)} = p_{\text{LV}}^{(j-1)} - \Delta p_{\text{LV}}^{(j)}$ and $p_{\text{RV}}^{(j)} = p_{\text{RV}}^{(j-1)} - \Delta p_{\text{RV}}^{(j)}$.
- When the convergence criterion (based on the increment) is satisfied, we set
  $\mathbf{d}_{\text{h}}^{n+1} = \mathbf{d}_{\text{h}}^{(j)}$, $p_{\text{LV}}^{n+1} = p_{\text{LV}}^{(j)}$ and $p_{\text{RV}}^{n+1} = p_{\text{RV}}^{(j)}$.

We solve the saddle-point problem (16) via Schur complement reduction [105]. Specifically, system (7) can be written as

$$\begin{cases} J_{\mathbf{d},\mathbf{d}} \Delta\mathbf{d}_{\text{h}} + J_{\mathbf{d},p_{\text{LV}}} \Delta p_{\text{LV}} + J_{\mathbf{d},p_{\text{RV}}} \Delta p_{\text{RV}} = \mathbf{r}_{\mathbf{d}} \\ J_{p_{\text{LV}},\mathbf{d}} \Delta\mathbf{d}_{\text{h}} = r_{p_{\text{LV}}} \\ J_{p_{\text{RV}},\mathbf{d}} \Delta\mathbf{d}_{\text{h}} = r_{p_{\text{RV}}} \end{cases} \tag{17}$$

where for simplicity we omit the superscript (j). Deriving $\Delta\mathbf{d}_{\mathrm{h}}$ from the first equation of (17) we have

$$\begin{cases} \Delta\mathbf{d}_{\mathrm{h}} = \mathbf{v} - \mathbf{w}_{\mathrm{L}}\Delta p_{\mathrm{LV}} - \mathbf{w}_{\mathrm{R}}\Delta p_{\mathrm{RV}} \\ \alpha_{\mathrm{LL}}\Delta p_{\mathrm{LV}} + \alpha_{\mathrm{LR}}\Delta p_{\mathrm{RV}} = b_{\mathrm{L}} \\ \alpha_{\mathrm{RL}}\Delta p_{\mathrm{LV}} + \alpha_{\mathrm{RR}}\Delta p_{\mathrm{RV}} = b_{\mathrm{R}} \end{cases} \tag{18}$$

where

$$\alpha_{\mathrm{LL}} = J_{p_{\mathrm{LV}},\mathbf{d}}\mathbf{w}_{\mathrm{L}}, \qquad \alpha_{\mathrm{LR}} = J_{p_{\mathrm{LV}},\mathbf{d}}\mathbf{w}_{\mathrm{R}}, \qquad \alpha_{\mathrm{RL}} = J_{p_{\mathrm{RV}},\mathbf{d}}\mathbf{w}_{\mathrm{L}}, \qquad \alpha_{\mathrm{RR}} = J_{p_{\mathrm{RV}},\mathbf{d}}\mathbf{w}_{\mathrm{R}},$$

$$b_{\mathrm{L}} = J_{p_{\mathrm{LV}},\mathbf{d}}\mathbf{v} - r_{p_{\mathrm{LV}}}, \qquad b_{\mathrm{R}} = J_{p_{\mathrm{RV}},\mathbf{d}}\mathbf{v} - r_{p_{\mathrm{RV}}},$$

with

$$\mathbf{w}_{\mathrm{L}} = J^{-1}_{\mathbf{d},\mathbf{d}}J_{\mathbf{d},p_{\mathrm{LV}}} \qquad \mathbf{w}_{\mathrm{R}} = J^{-1}_{\mathbf{d},\mathbf{d}}J_{\mathbf{d},p_{\mathrm{RV}}}, \qquad \mathbf{v} = J^{-1}_{\mathbf{d},\mathbf{d}}\mathbf{r}_{\mathbf{d}}. \tag{19}$$

Solving Eq. (18) we obtain

$$\begin{aligned} &\Delta\mathbf{d}_{\mathrm{h}} = \mathbf{v} - \mathbf{w}_{\mathrm{L}}\Delta p_{\mathrm{LV}} - \mathbf{w}_{\mathrm{R}}\Delta p_{\mathrm{RV}}, \\ &\Delta p_{\mathrm{LV}} = \frac{b_{\mathrm{L}}\alpha_{\mathrm{RR}} + b_{\mathrm{R}}\alpha_{\mathrm{LR}}}{\alpha_{\mathrm{LL}}\alpha_{\mathrm{RR}} - \alpha_{\mathrm{RL}}\alpha_{\mathrm{LR}}}, \quad \Delta p_{\mathrm{RV}} = \frac{b_{\mathrm{R}}\alpha_{\mathrm{LL}} + b_{\mathrm{L}}\alpha_{\mathrm{RL}}}{\alpha_{\mathrm{LL}}\alpha_{\mathrm{RR}} - \alpha_{\mathrm{RL}}\alpha_{\mathrm{LR}}}. \end{aligned} \tag{20}$$

Notice that we have to solve three linear systems (19) in order to obtain the solution (20).

References

[1] V. Gurev, T. Lee, J. Constantino, H. Arevalo, N. Trayanova, Models of cardiac electromechanics based on individual hearts imaging data, Biomech. Model. Mechanobiol. 10 (3) (2011) 295–306.

[2] C. Augustin, A. Neic, M. Liebmann, A. Prassl, S. Niederer, G. Haase, G. Plank, Anatomically accurate high resolution modeling of human whole heart electromechanics: a strongly scalable algebraic multigrid solver method for nonlinear deformation, J. Comput. Phys. 305 (2016) 622–646.

[3] C. Augustin, T. Fastl, A. Neic, C. Bellini, J. Whitaker, R. Rajani, M. O'Neill, M. Bishop, G. Plank, S. Niederer, The impact of wall thickness and curvature on wall stress in patient-specific electromechanical models of the left atrium, Biomech. Model. Mechanobiol. 19 (3) (2020) 1015–1034.

[4] S. Land, S. Niederer, Influence of atrial contraction dynamics on cardiac function, Int. J. Numer. Methods Biomed. Eng. 34 (3) (2018) e2931.

[5] D. Nordsletten, S. Niederer, M. Nash, P. Hunter, N. Smith, Coupling multi-physics models to cardiac mechanics, Prog. Biophys. Mol. Biol. 104 (2011) 77–88.

[6] M. Strocchi, C. Augustin, M. Gsell, E. Karabelas, A. Neic, K. Gillette, O. Razeghi, A. Prassl, E. Vigmond, J. Behar, et al., A publicly available virtual cohort of four-chamber heart meshes for cardiac electro-mechanics simulations, PLoS One 15 (2020) e0235145.

[7] T. Gerach, S. Schuler, J. Fröhlich, L. Lindner, E. Kovacheva, R. Moss, E. Wülfers, G. Seemann, C. Wieners, A. Loewe, Electro-mechanical whole-heart digital twins: A fully coupled multi-physics approach, Mathematics 9 (11) (2021).

[8] M. Sermesant, R. Chabiniok, P. Chinchapatnam, T. Mansi, F. Billet, P. Moireau, J. Peyrat, K. Wong, J. Relan, K. Rhode, et al., Patient-specific electromechanical models of the heart for the prediction of pacing acute effects in CRT: a preliminary clinical validation, Med. Image Anal. 16 (1) (2012) 201–215.

[9] M. Peirlinck, F. Costabal, J. Yao, J. Guccione, S. Tripathy, Y. Wang, D. Ozturk, P. Segars, T. Morrison, S. Levine, et al., Precision medicine in human heart modeling, Biomech. Model. Mechanobiol. (2021) 1–29.

[10] N. Smith, D. Nickerson, E. Crampin, P. Hunter, Multiscale computational modelling of the heart, Acta Numer. 13 (2004) 371.

[11] R. Chabiniok, V. Wang, M. Hadjicharalambous, L. Asner, J. Lee, M. Sermesant, E. Kuhl, A. Young, P. Moireau, M. Nash, et al., Multiphysics and multiscale modelling, data–model fusion and integration of organ physiology in the clinic: ventricular cardiac mechanics, Interface Focus 6 (2) (2016) 20150083.

[12] E. Crampin, M. Halstead, P. Hunter, P. Nielsen, D. Noble, N. Smith, M. Tawhai, Computational physiology and the physiome project, Exp. Physiol. 89 (1) (2004) 1–26.

[13] L. Marx, M. Gsell, A. Rund, F. Caforio, A. Prassl, G. Toth-Gayor, T. Kuehne, C. Augustin, G. Plank, Personalization of electro-mechanical models of the pressure-overloaded left ventricle: fitting of windkessel-type afterload models, Phil. Trans. R. Soc. A 378 (2173) (2020) 20190342.

[14] A. Gerbi, L. Dede', A. Quarteroni, A monolithic algorithm for the simulation of cardiac electromechanics in the human left ventricle, Math. Eng. 1 (2018).

[15] F. Regazzoni, M. Salvador, P.C. Africa, M. Fedele, L. Dede', A. Quarteroni, A cardiac electromechanics model coupled with a lumped parameters model for closed-loop blood circulation. Part I: model derivation, 2020, http://arxiv.org/abs/2011.15040.

[16] M. Salvador, L. Dedè, A. Quarteroni, An intergrid transfer operator using radial basis functions with application to cardiac electromechanics, Comput. Mech. 66 (2020) 491–511.
[17] F. Levrero-Florencio, F. Margara, E. Zacur, A. Bueno-Orovio, Z. Wang, A. Santiago, J. Aguado-Sierra, G. Houzeaux, V. Grau, D. Kay, et al., Sensitivity analysis of a strongly-coupled human-based electromechanical cardiac model: Effect of mechanical parameters on physiologically relevant biomarkers, Comput. Methods Appl. Mech. Eng. 361 (2020) 112762.
[18] A. Propp, A. Gizzi, F. Levrero-Florencio, R. Ruiz-Baier, An orthotropic electro-viscoelastic model for the heart with stress-assisted diffusion, Biomech. Model. Mechanobiol. 19 (2) (2020) 633–659.
[19] S. Rossi, T. Lassila, R. Ruiz-Baier, A. Sequeira, A. Quarteroni, Thermodynamically consistent orthotropic activation model capturing ventricular systolic wall thickening in cardiac electromechanics, Eur. J. Mech.-A/Solids 48 (2014) 129–142.
[20] A. Palit, S. Bhudia, T. Arvanitis, G. Turley, M. Williams, Computational modelling of left-ventricular diastolic mechanics: Effect of fibre orientation and right-ventricle topology, J. Biomech. 48 (4) (2015) 604–612.
[21] M. Sermesant, K. Rhode, G. Sanchez-Ortiz, O. Camara, R. Andriantsimiavona, S. Hegde, D. Rueckert, P. Lambiase, C. Bucknall, E. Rosenthal, et al., Simulation of cardiac pathologies using an electromechanical biventricular model and XMR interventional imaging, Med. Image Anal. 9 (5) (2005) 467–480.
[22] D. Chapelle, M. Fernández, J. Gerbeau, P. Moireau, J. Sainte-Marie, N. Zemzemi, Numerical simulation of the electromechanical activity of the heart, in: International Conference on Functional Imaging and Modeling of the Heart, Springer, 2009, pp. 357–365.
[23] S. Göktepe, E. Kuhl, Electromechanics of the heart: a unified approach to the strongly coupled excitation–contraction problem, Comput. Mech. 45 (2) (2010) 227–243.
[24] A. Crozier, C. Augustin, A. Neic, A. Prassl, M. Holler, T. Fastl, A. Hennemuth, K. Bredies, T. Kuehne, M. Bishop, et al., Image-based personalization of cardiac anatomy for coupled electromechanical modeling, Ann. Biomed. Eng. 44 (1) (2016) 58–70.
[25] M. Hirschvogel, M. Bassilious, L. Jagschies, S. Wildhirt, M. Gee, A monolithic 3D-0D coupled closed-loop model of the heart and the vascular system: experiment-based parameter estimation for patient-specific cardiac mechanics, Int. J. Numer. Methods Biomed. Eng. 33 (2017) e2842.
[26] A. Ahmad Bakir, A. Al Abed, M. Stevens, N. Lovell, S. Dokos, A multiphysics biventricular cardiac model: Simulations with a left-ventricular assist device, Front. Physiol. 9 (2018) 1259.
[27] E. Garcia-Blanco, R. Ortigosa, A. Gil, J. Bonet, Towards an efficient computational strategy for electro-activation in cardiac mechanics, Comput. Methods Appl. Mech. Eng. 356 (2019) 220–260.
[28] C. Augustin, M. Gsell, E. Karabelas, E. Willemen, F. Prinzen, J. Lumens, E. Vigmond, G. Plank, A computationally efficient physiologically comprehensive 3D–0d closed-loop model of the heart and circulation, Comput. Methods Appl. Mech. Eng. 386 (2021) 114092.
[29] R. Kerckhoffs, M. Neal, Q. Gu, J. Bassingthwaighte, J. Omens, A. McCulloch, Coupling of a 3D finite element model of cardiac ventricular mechanics to lumped systems models of the systemic and pulmonic circulation, Ann. Biomed. Eng. 35 (2007) 1–18.
[30] L. Dedè, F. Regazzoni, C. Vergara, P. Zunino, M. Guglielmo, R. Scrofani, L. Fusini, C. Cogliati, G. Pontone, A. Quarteroni, Modeling the cardiac response to hemodynamic changes associated with COVID-19: a computational study, Math. Biosci. Eng. 18 (4) (2021) 3364–3383.
[31] D. Guan, J. Yao, X. Luo, H. Gao, Effect of myofibre architecture on ventricular pump function by using a neonatal porcine heart model: from DT-MRI to rule-based methods, R. Soc. Open Sci. 7 (4) (2020) 191655.
[32] Z. Wang, A. Santiago, X. Zhou, L. Wang, F. Margara, F. Levrero-Florencio, A. Das, C. Kelly, E. Dall'Armellina, M. Vazquez, et al., Human biventricular electromechanical simulations on the progression of electrocardiographic and mechanical abnormalities in post-myocardial infarction, EP Eur. 23 (Supplement_1) (2021) i143–i152.
[33] G. Elzinga, N. Westerhof, Pressure and flow generated by the left ventricle against different impedances, Circ. Res. 32 (2) (1973) 178–186.
[34] H. Liu, F. Liang, J. Wong, T. Fujiwara, W. Ye, K. Tsubota, M. Sugawara, Multi-scale modeling of hemodynamics in the cardiovascular system, Acta Mech. Sinica 31 (4) (2015) 446–464.
[35] P. Segers, E. Rietzschel, M. De Buyzere, N. Stergiopulos, N. Westerhof, L. Van Bortel, T. Gillebert, P. Verdonck, Three-and four-element windkessel models: assessment of their fitting performance in a large cohort of healthy middle-aged individuals, Proc. Inst. Mech. Eng. H 222 (4) (2008) 417–428.
[36] N. Stergiopulos, B. Westerhof, N. Westerhof, Total arterial inertance as the fourth element of the Windkessel model, Am. J. Physiol.-Heart Circul. Physiol. 276 (1) (1999) H81–H88.
[37] J. Wang, A. O'Brien, N. Shrive, K. Parker, J. Tyberg, Time-domain representation of ventricular-arterial coupling as a windkessel and wave system, Am. J. Physiol.-Heart Circul. Physiol. 284 (4) (2003) H1358–H1368.
[38] N. Westerhof, G. Elzinga, Normalized input impedance and arterial decay time over heart period are independent of animal size, Am. J. Physiol.-Regul., Integr. Comparat. Physiol. 261 (1) (1991) R126–R133.
[39] L. Dedè, A. Gerbi, A. Quarteroni, Segregated algorithms for the numerical simulation of cardiac electromechanics in the left human ventricle, in: D. Ambrosi, P. Ciarletta (Eds.), The Mathematics of Mechanobiology, Springer, 2020, pp. 81–116.
[40] T. Eriksson, A.J. Prassl, G. Plank, G. Holzapfel, Influence of myocardial fiber/sheet orientations on left ventricular mechanical contraction, Math. Mech. Solids 18 (6) (2013) 592–606.
[41] T. Usyk, I. LeGrice, A. McCulloch, Computational model of three-dimensional cardiac electromechanics, Comput. Visual. Sci. 4 (4) (2002) 249–257.
[42] P. Blanco, R. Feijóo, et al., A 3D-1d-0D computational model for the entire cardiovascular system, Comput. Mech. 29 (2010) 5887–5911.
[43] T. Arts, T. Delhaas, P. Bovendeerd, X. Verbeek, F. Prinzen, Adaptation to mechanical load determines shape and properties of heart and circulation: the CircAdapt model, Am. J. Physiol.-Heart Circul. Physiol. 288 (2005) H1943–H1954.

[44] M. Neal, J. Bassingthwaighte, Subject-specific model estimation of cardiac output and blood volume during hemorrhage, Cardiovascul. Eng. 7 (3) (2007) 97–120.
[45] S. Paeme, K. Moorhead, J. Chase, B. Lambermont, P. Kolh, V. D'orio, L. Pierard, M. Moonen, P. Lancellotti, P. Dauby, et al., Mathematical multi-scale model of the cardiovascular system including mitral valve dynamics. Application to ischemic mitral insufficiency, Biomed. Eng. Online 10 (1) (2011) 1–20.
[46] F. Regazzoni, M. Salvador, P.C. Africa, M. Fedele, L. Dede', A. Quarteroni, A cardiac electromechanics model coupled with a lumped parameters model for closed-loop blood circulation. Part II: numerical approximation, 2020, http://arxiv.org/abs/2011.15051.
[47] R. Piersanti, P. Africa, M. Fedele, C. Vergara, L. Dedè, A. Corno, A. Quarteroni, Modeling cardiac muscle fibers in ventricular and atrial electrophysiology simulations, Comput. Methods Appl. Mech. Eng. 373 (2021) 113468.
[48] D.D. Streeter Jr., H.M. Spotnitz, D.P. Patel, J. Ross Jr., E.H. Sonnenblick, Fiber orientation in the canine left ventricle during diastole and systole, Circ. Res. 24 (3) (1969) 339–347.
[49] D.E. Roberts, L.T. Hersh, A.M. Scher, Influence of cardiac fiber orientation on wavefront voltage, conduction velocity, and tissue resistivity in the dog, Circ. Res. 44 (5) (1979) 701–712.
[50] D. Gil, R. Aris, A. Borras, E. Ramírez, R. Sebastian, M. Vázquez, Influence of fiber connectivity in simulations of cardiac biomechanics, Int. J. Comput. Assist. Radiol. Surgery 14 (1) (2019) 63–72.
[51] F. Carreras, J. Garcia-Barnes, D. Gil, S. Pujadas, C. Li, R. Suarez-Arias, R. Leta, X. Alomar, M. Ballester, G. Pons-Llado, Left ventricular torsion and longitudinal shortening: two fundamental components of myocardial mechanics assessed by tagged cine-MRI in normal subjects, Int. J. Cardiovasc. Imaging 28 (2) (2012) 273–284.
[52] J. Bayer, R. Blake, G. Plank, N. Trayanova, A novel rule-based algorithm for assigning myocardial fiber orientation to computational heart models, Ann. Biomed. Eng. 40 (10) (2012) 2243–2254.
[53] J. Wong, E. Kuhl, Generating fibre orientation maps in human heart models using Poisson interpolation, Comput. Methods Biomech. Biomed. Eng. 17 (11) (2014) 1217–1226.
[54] R. Doste, D. Soto-Iglesias, G. Bernardino, A. Alcaine, R. Sebastian, S. Giffard-Roisin, M. Sermesant, A. Berruezo, D. Sanchez-Quintana, O. Camara, A rule-based method to model myocardial fiber orientation in cardiac biventricular geometries with outflow tracts, Int. J. Numer. Methods Biomed. Eng. 35 (4) (2019) e3185.
[55] A. Quarteroni, T. Lassila, S. Rossi, R. Ruiz-Baier, Integrated heart—Coupling multiscale and multiphysics models for the simulation of the cardiac function, Comput. Methods Appl. Mech. Eng. 314 (2017) 345–407.
[56] L. Azzolin, L. Dedè, A. Gerbi, A. Quarteroni, Effect of fibre orientation and bulk modulus on the electromechanical modelling of human ventricles, Math. Eng. 2 (4) (2020) 614–638.
[57] M. Pluijmert, T. Delhaas, A. De la Parra, W. Kroon, F. Prinzen, P. Bovendeerd, Determinants of biventricular cardiac function: a mathematical model study on geometry and myofiber orientation, Biomech. Model. Mechanobiol. 16 (2) (2017) 721–729.
[58] D. Guan, X. Zhuan, W. Holmes, X. Luo, H. Gao, Modelling of fibre dispersion and its effects on cardiac mechanics from diastole to systole, J. Eng. Math. 128 (1) (2021) 1–24.
[59] F. Ahmad, S. Soe, N. White, R. Johnston, I. Khan, J. Liao, M. Jones, R. Prabhu, I. Maconochie, P. Theobald, Region-specific microstructure in the neonatal ventricles of a porcine model, Ann. Biomed. Eng. 46 (12) (2018) 2162–2176.
[60] G. Sommer, A. Schriefl, M. Andrä, M. Sacherer, C. Viertler, H. Wolinski, G. Holzapfel, Biomechanical properties and microstructure of human ventricular myocardium, Acta Biomater. 24 (2015) 172–192.
[61] D. Lin, F. Yin, A multiaxial constitutive law for mammalian left ventricular myocardium in steady-state barium contracture or tetanus, J. Biomech. Eng. 120 (4) (1998) 504–517.
[62] M. Genet, L. Lee, R. Nguyen, H. Haraldsson, G. Acevedo-Bolton, Z. Zhang, L. Ge, K. Ordovas, S. Kozerke, J. Guccione, Distribution of normal human left ventricular myofiber stress at end diastole and end systole: a target for in silico design of heart failure treatments, J. Appl. Physiol. 117 (2) (2014) 142–152.
[63] K. Sack, E. Aliotta, D. Ennis, J. Choy, G. Kassab, J. Guccione, T. Franz, Construction and validation of subject-specific biventricular finite-element models of healthy and failing swine hearts from high-resolution DT-MRI, Front. Physiol. 9 (2018) 539.
[64] J. Wenk, D. Klepach, L. Lee, Z. Zhang, L. Ge, E. Tseng, A. Martin, S. Kozerke, J. Gorman III, R. Gorman, et al., First evidence of depressed contractility in the border zone of a human myocardial infarction, Ann. Thoracic Surgery 93 (4) (2012) 1188–1193.
[65] T. Eriksson, A. Prassl, G. Plank, G. Holzapfel, Modeling the dispersion in electromechanically coupled myocardium, Int. J. Numer. Methods Biomed. Eng. 29 (11) (2013) 1267–1284.
[66] A. Maceira, S. Prasad, M. Khan, D. Pennell, Normalized left ventricular systolic and diastolic function by steady state free precession cardiovascular magnetic resonance, J. Cardiovasc. Magn. Resonance 8 (3) (2006) 417–426.
[67] G. Tamborini, N. Marsan, P. Gripari, F. Maffessanti, D. Brusoni, M. Muratori, E. Caiani, C. Fiorentini, M. Pepi, Reference values for right ventricular volumes and ejection fraction with real-time three-dimensional echocardiography: evaluation in a large series of normal subjects, J. Am. Soc. Echocardiogr. 23 (2) (2010) 109–115.
[68] A. Maceira, S. Prasad, M. Khan, D. Pennell, Reference right ventricular systolic and diastolic function normalized to age, gender and body surface area from steady-state free precession cardiovascular magnetic resonance, Eur. Heart J. 27 (23) (2006) 2879–2888.
[69] T. Sugimoto, R. Dulgheru, A. Bernard, F. Ilardi, L. Contu, K. Addetia, L. Caballero, N. Akhaladze, G. Athanassopoulos, D. Barone, et al., Echocardiographic reference ranges for normal left ventricular 2d strain: results from the EACVI NORRE study, Eur. Heart J.-Cardiovasc. Imaging 18 (8) (2017) 833–840.
[70] A. Bishop, P. White, P. Oldershaw, R. Chaturvedi, C. Brookes, A. Redington, Clinical application of the conductance catheter technique in the adult human right ventricle, Int. J. Cardiol. 58 (3) (1997) 211–221.
[71] K. Emilsson, R. Egerlid, B. Nygren, B. Wandt, Mitral annulus motion versus long-axis fractional shortening, Exp. Clin. Cardiol. 11 (4) (2006) 302.

[72] U. Sechtem, B. Sommerhoff, W. Markiewicz, R. White, M. Cheitlin, C. Higgins, Regional left ventricular wall thickening by magnetic resonance imaging: evaluation in normal persons and patients with global and regional dysfunction, Am. J. Cardiol. 59 (1) (1987) 145–151.
[73] A. Lee, U. Nguyen, O. Razeghi, J. Gould, B. Sidhu, B. Sieniewicz, J. Behar, M. Mafi-Rad, G. Plank, F. Prinzen, et al., A rule-based method for predicting the electrical activation of the heart with cardiac resynchronization therapy from non-invasive clinical data, Med. Image Anal. 57 (2019) 197–213.
[74] J. Bayer, J. Beaumont, A. Krol, Laplace–Dirichlet energy field specification for deformable models. an FEM approach to active contour fitting, Ann. Biomed. Eng. 33 (9) (2005) 1175–1186.
[75] P. Colli-Franzone, L. Pavarino, S. Scacchi, Mathematical Cardiac Electrophysiology, Vol. 13, Springer, 2014.
[76] P. Colli-Franzone, L. Pavarino, S. Scacchi, A numerical study of scalable cardiac electro-mechanical solvers on HPC architectures, Front. Physiol. 9 (2018) 268.
[77] F. Nobile, A. Quarteroni, R. Ruiz-Baier, An active strain electromechanical model for cardiac tissue, Int. J. Numer. Methods Biomed. Eng. 28 (2012) 52–71.
[78] S. Niederer, G. Plank, P. Chinchapatnam, M. Ginks, P. Lamata, K. Rhode, C. Rinaldi, R. Razavi, N. Smith, Length-dependent tension in the failing heart and the efficacy of cardiac resynchronization therapy, Cardiovasc. Res. 89 (2011) 336–343.
[79] R. Ruiz-Baier, A. Gizzi, S. Rossi, C. Cherubini, A. Laadhari, S. Filippi, A. Quarteroni, Mathematical modelling of active contraction in isolated cardiomyocytes, Math. Med. Biol. 31 (2014) 259–283.
[80] S. Land, S. Park-Holohan, N. Smith, C. Dos Remedios, J. Kentish, S. Niederer, A model of cardiac contraction based on novel measurements of tension development in human cardiomyocytes, J. Molecular Cellular Cardiol. 106 (2017) 68–83.
[81] F. Regazzoni, L. Dedè, A. Quarteroni, Biophysically detailed mathematical models of multiscale cardiac active mechanics, PLoS Comput. Biol. 16 (2020) e1008294.
[82] F. Regazzoni, L. Dedè, A. Quarteroni, Machine learning of multiscale active force generation models for the efficient simulation of cardiac electromechanics, Comput. Methods Appl. Mech. Eng. 370 (2020) 113268.
[83] J. Guccione, A. McCulloch, L. Waldman, Passive material properties of intact ventricular myocardium determined from a cylindrical model, J. Biomech. Eng. 113 (1991) 42–55.
[84] J. Guccione, A. McCulloch, Finite element modeling of ventricular mechanics, in: Theory of Heart, Springer, 1991, pp. 121–144.
[85] R. Ogden, Non-Linear Elastic Deformations, Courier Corporation, 1997.
[86] G. Holzapfel, R. Ogden, Constitutive modelling of passive myocardium: a structurally based framework for material characterization, Philos. Trans. R. Soc. Lond. Ser. A Math. Phys. Eng. Sci. 367 (2009) 3445–3475.
[87] A. Quarteroni, A. Veneziani, C. Vergara, Geometric multiscale modeling of the cardiovascular system, between theory and practice, Comput. Methods Appl. Mech. Eng. 302 (2016) 193–252.
[88] C. Vergara, S. Palamara, D. Catanzariti, F. Nobile, E. Faggiano, C. Pangrazzi, M. Centonze, M. Maines, A. Quarteroni, G. Vergara, Patient-specific generation of the purkinje network driven by clinical measurements of a normal propagation, Med. Biol. Eng. Comput. 52 (2014) 813–826.
[89] F. Costabal, D. Hurtado, E. Kuhl, Generating purkinje networks in the human heart, J. Biomech. 49 (2016) 2455–2465.
[90] M. Landajuela, C. Vergara, A. Gerbi, L. Dedè, L. Formaggia, A. Quarteroni, Numerical approximation of the electromechanical coupling in the left ventricle with inclusion of the purkinje network, Int. J. Numer. Methods Biomed. Eng. 34 (2018) e2984.
[91] K. ten Tusscher, A. Panfilov, Alternans and spiral breakup in a human ventricular tissue model, Am. J. Physiol.-Heart Circul. Physiol. 291 (2006) H1088–H1100.
[92] F. Regazzoni, L. Dedè, A. Quarteroni, Active contraction of cardiac cells: a reduced model for sarcomere dynamics with cooperative interactions, Biomech. Model. Mechanobiol. 17 (2018) 1663–1686.
[93] D. Bers, Excitation-Contraction Coupling and Cardiac Contractile Force, Vol. 237, Springer Science & Business Media, 2001.
[94] S. Peng, W. Chang, A compressible approach in finite element analysis of rubber-elastic materials, Comput. Struct. 62 (1997) 573–593.
[95] S. Doll, K. Schweizerhof, On the development of volumetric strain energy functions, J. Appl. Mech. 67 (2000) 17–21.
[96] A. Gerbi, L. Dedè, A. Quarteroni, A monolithic algorithm for the simulation of cardiac electromechanics in the human left ventricle, Math. Eng. 1 (2018) 1–37.
[97] M. Pfaller, J. Hörmann, M. Weigl, A. Nagler, R. Chabiniok, C. Bertoglio, W. Wall, The importance of the pericardium for cardiac biomechanics: from physiology to computational modeling, Biomech. Model. Mechanobiol. 18 (2019) 503–529.
[98] M. Strocchi, M. Gsell, C. Augustin, O. Razeghi, C. Roney, A. Prassl, E. Vigmond, J. Behar, J. Gould, C. Rinaldi, et al., Simulating ventricular systolic motion in a four-chamber heart model with spatially varying robin boundary conditions to model the effect of the pericardium, J. Biomech. 101 (2020) 109645.
[99] A. Quarteroni, L. Dedè, A. Manzoni, C. Vergara, Mathematical Modelling of the Human Cardiovascular System: Data, Numerical Approximation, Clinical Applications, in: Cambridge Monographs on Applied and Computational Mathematics, Cambridge University Press, 2019.
[100] A. Quarteroni, Numerical Models for Differential Problems, Vol. 2, Springer, 2009.
[101] P. Africa, Scalable adaptive simulation of organic thin-film transistors, (Ph.D. thesis), Politecnico di Milano, 2019.
[102] B. Carsten, C. Lucas, G. Omar, `P4est`: Scalable algorithms for parallel adaptive mesh refinement on forests of octrees, SIAM J. Sci. Comput. 33 (2011) 1103–1133.
[103] A. Quarteroni, R. Sacco, F. Saleri, Numerical Mathematics, Vol. 37, Springer Science & Business Media, 2010.
[104] S. Niederer, L. Mitchell, N. Smith, G. Plank, Simulating human cardiac electrophysiology on clinical time-scales, Front. Physiol. 2 (2011) 14.
[105] M. Benzi, G. Golub, J. Liesen, et al., Numerical solution of saddle point problems, Acta Numer. 14 (2005) 1–137.

[106] F. Regazzoni, A. Quarteroni, Accelerating the convergence to a limit cycle in 3D cardiac electromechanical simulations through a data-driven 0D emulator, Comput. Biol. Med. (2021) 104641.
[107] Z.M.G. Inc., Zygote solid 3d heart generation II developement report, Technical Report, 2014.
[108] L. Antiga, M. Piccinelli, L. Botti, B. Ene-Iordache, A. Remuzzi, D. Steinman, An image-based modeling framework for patient-specific computational hemodynamics, Med. Biol. Eng. Comput. 46 (11) (2008) 1097–1112.
[109] M. Fedele, A. Quarteroni, Polygonal surface processing and mesh generation tools for the numerical simulation of the cardiac function, Int. J. Numer. Methods Biomed. Eng. 37 (4) (2021) e3435.
[110] D. Durrer, R. Van Dam, G. Freud, M. Janse, F. Meijler, R. Arzbaecher, Total excitation of the isolated human heart, Circulation 41 (6) (1970) 899–912.
[111] D. Arndt, W. Bangerth, T. Clevenger, D. Davydov, M. Fehling, D. Garcia-Sanchez, G. Harper, T. Heister, L. Heltai, M. Kronbichler, R. Kynch, M. Maier, J.-P. Pelteret, B. Turcksin, D. Wells, The `deal.II` library, version 9.1, J. Numer. Math. (2019).
[112] H. Lombaert, J. Peyrat, P. Croisille, S. Rapacchi, L. Fanton, F. Cheriet, P. Clarysse, I. Magnin, H. Delingette, N. Ayache, Human atlas of the cardiac fiber architecture: study on a healthy population, IEEE Trans. Med. Imaging 31 (7) (2012) 1436–1447.
[113] R. Anderson, M. Smerup, D. Sanchez-Quintana, M. Loukas, P. Lunkenheimer, The three-dimensional arrangement of the myocytes in the ventricular walls, Clin. Anatomy: Off. J. Am. Assoc. Clin. Anatomists Br. Assoc. Clin. Anatomists 22 (1) (2009) 64–76.
[114] M. Salvador, M. Fedele, P. Africa, E. Sung, L. Dede', A. Prakosa, J. Chrispin, N. Trayanova, A. Quarteroni, Electromechanical modeling of human ventricles with ischemic cardiomyopathy: numerical simulations in sinus rhythm and under arrhythmia, Comput. Biol. Med. 136 (2021) 104674.
[115] H. Finsberg, C. Xi, J.L. Tan, L. Zhong, M. Genet, J. Sundnes, L. Lee, S. Wall, Efficient estimation of personalized biventricular mechanical function employing gradient-based optimization, Int. J. Numer. Methods Biomed. Eng. 34 (7) (2018) e2982.
[116] M. Carlsson, M. Ugander, H. Mosén, T. Buhre, H. Arheden, Atrioventricular plane displacement is the major contributor to left ventricular pumping in healthy adults, athletes, and patients with dilated cardiomyopathy, Am. J. Physiol.-Heart Circul. Physiol. 292 (3) (2007) H1452–H1459.